



UNIVERSITÀ  
DI PAVIA



UNIVERSITY OF PAVIA  
FACULTY OF ENGINEERING

UNIVERSITY SCHOOL OF ADVANCED  
STUDIES - IUSS PAVIA

**Post Lateral-Torsional Buckling Behaviour of a Simply-Supported Beam Subjected to Midspan Point Load**

A Thesis Submitted in Partial Fulfilment of the Requirements  
for the Degree of Master of Science (Laurea Magistrale) in

Civil Engineering for the Mitigation of Risk from Natural Hazards

by

**Wendwesen Fekede Haile**

Supervisors: Prof. Richard Wiebe, University of Washington

Prof. Gerard J. O'Reilly, IUSS Pavia

September 2025



## ABSTRACT

Lateral-torsional buckling (LTB) is a critical instability phenomenon in slender beams subjected to major axis bending, involving both lateral displacement and torsional rotation. Although the critical buckling load has been widely studied, the nonlinear post-buckling response of beams has gathered less attention.

This thesis investigates the LTB behavior of simply-supported European rolled I-section (IPE) beams subjected to midspan point load. Beam profiles of IPE 120 to IPE 300 with unbraced span lengths varying from 2.0 m to 6.0 m and with “fork-type” restraint, that prevents twist of cross-section, are examined. The study examines both the critical buckling load and the post-buckling response of the beams neglecting cross-section warping.

Two analytical models employing energy-based formulations derived from the principle of minimum potential energy assuming circular and parabolic deformation paths are employed with a goal of developing accurate analytical solutions. These models provide expressions for load as a function of displacement and twist, offering insight into the beam’s buckling and post-buckling behavior. In parallel, a nonlinear numerical finite element model (FEM) is developed in OpenSeesPy to simulate the LTB behavior. The study includes a comparison of critical buckling load obtained from analytical methods, the developed numerical model and the Eurocode formulation. The emphasis of the work is placed on a comparison of post-buckling response from the analytical methods and FEM with the responses from OpenSeesPy simulations served as reliable numerical benchmark.

Results obtained for various IPE sections and beam spans indicate that while the analytical circular deformation path model provides a critical buckling load expression which exhibits a strong resemblance with the Eurocode formulation, it tends to overestimate the critical load by roughly 105% compared to the numerical model. Moreover, its post-buckling response shows softening behavior unlike the numerical model and its deformed shapes completely disagree with the numerical solutions, even though they are qualitatively similar. In contrast, Eurocode critical buckling load predictions, used alongside the numerical and analytical results for comparison, underestimate the numerical results by about 12%.

A parabolic deformation path model is developed, with a coefficient determined based on the numerical critical load, to solve the problem of unmatched critical load and post-buckling behavior of the circular path model. Post-buckling responses are examined using

load-deflection and load-twist curves. The post-buckling response results from the numerical model shows hardening behavior with a nearly elliptical deformed shape while the responses from the parabolic path with the calibrated coefficients shows hardening behavior with deformed shapes converging initially towards the numerical results for intermediate beam cross-sections and spans.

Overall, this study highlights the capabilities and limitations of simplified analytical models for capturing post-LTB behavior, offering valuable comparisons with code-based and numerical simulation. With further study including material nonlinearity, warping effects, and other imperfections it can be applied for practical analysis and design.

## **ACKNOWLEDGEMENTS**

First and foremost, I would like to express my deepest gratitude to God for His endless blessings throughout my life. I am sincerely thankful to my supervisors, Professor Richard Wiebe and Professor Gerard J. O'Reilly, for their support, valuable guidance, and encouragement throughout my research. Their expertise and insights have been helpful to the completion of this work. I would also like to extend my heartfelt thanks to all my professors at the University of Pavia and IUSS Pavia for their continuous assistance and support throughout my academic journey. A special thank you goes to my family and friends, whose love, encouragement, and belief in me have been a strength. I am grateful for their presence in my life. Lastly, I would like to express my gratitude to all my classmates for making the past two years memorable and inspiring. A special thanks to my dear friend, Yalemnigus Fufa, for being there for me whenever I needed help and support.



## TABLE OF CONTENTS

ABSTRACT .....	iii
ACKNOWLEDGEMENTS .....	v
TABLE OF CONTENTS .....	vii
LIST OF FIGURES .....	ix
LIST OF TABLES .....	xi
LIST OF SYMBOLS.....	xiii
1. INTRODUCTION.....	1
1.1 BACKGROUND .....	1
1.2 MOTIVATION .....	2
1.3 PROBLEM STATEMENT .....	2
1.4 OUTLINE OF THE THESIS.....	3
2. LITERATURE REVIEW .....	1
2.1 INTRODUCTION.....	1
2.2 ANALYTICAL STUDIES.....	1
2.3 DESIGN CODE RECOMMENDATION.....	1
2.4 MODIFICATION FACTORS .....	2
2.5 EXPERIMENTAL AND NUMERICAL STUDIES .....	3
3. ANALYTICAL MODELING .....	5
3.1 STRUCTURAL MODELLING AND PROCEDURE .....	5
3.2 DISCRETIZATION.....	6
3.2.1 Vertical Stiffness .....	6
3.2.2 Lateral Stiffness .....	7
3.2.3 Torsional Stiffness .....	7
3.3 GENERAL POTENTIAL ENERGY EQUATION.....	8
3.4 CIRCULAR DEFORMATION PATH .....	10

3.4.1	Minimization of Potential Energy .....	11
3.4.2	Equilibrium Path .....	12
3.5	PARABOLIC DEFORMATION PATH.....	13
3.5.1	Minimization of Potential Energy .....	14
3.5.2	Equilibrium Path .....	15
4.	NUMERICAL MODELING.....	17
4.1	STRUCTURAL MODELLING AND PROCEDURE.....	17
5.	RESULTS AND DISCUSSION.....	19
5.1	COMPARISON OF CRITICAL BUCKLING LOAD.....	19
5.1.1	Critical Buckling Load from Eurocode-3 Simplified Formula.....	19
5.1.2	Critical Buckling Load from Numerical Simulation (OpenSeesPy) .....	21
5.1.3	Critical Buckling Load from Analytical Circular Path Solution .....	21
5.1.4	Critical Buckling Load from Analytical Parabolic Path Solution.....	24
5.1.5	Comparison of Critical Buckling Load for Various IPE Sections.....	25
5.1.6	Comparison of Critical Buckling Load for Various Beam Spans .....	27
5.2	DETERMINATION OF THE COEFFICIENT OF PARABOLIC PATH SOLUTION .....	28
5.3	COMPARISON OF POST-BUCKLING RESPONSE .....	29
5.3.1	Comparison of Post-Buckling Response for Various IPE Sections .....	29
5.3.2	Comparison of Post-Buckling Response for Various Beam Spans.....	46
6.	CONCLUSIONS AND RECOMMENDATIONS .....	59
6.1	SUMMARY AND CONCLUSIONS .....	59
6.2	FUTURE WORK RECOMMENDATIONS .....	60
REFERENCES .....	63	
APPENDIX A. EQUATION OF PARABOLIC PATH.....	65	
APPENDIX B. NUMERICAL CODE IN OPENSEESESPY .....	66	

## LIST OF FIGURES

Figure 1.1. LTB of a simply-supported I-beam.....	1
Figure 1.2. Deformation of a simply-supported I-beam subjected to point load.....	3
Figure 3.1. Simply-supported beam subjected to point load at midspan.....	5
Figure 3.2. Vertical deflection of simply-supported beam due to vertical point load.....	6
Figure 3.3. Twist of simply-supported beam due to torsional moment.....	7
Figure 3.4. Discritization of simply-supported beam subjected to point load.....	8
Figure 3.5. Assumed deformed orientation of the cross-section for the two paths. ....	9
Figure 4.1. Numerical model of simply-supported beam subjected to point load.....	18
Figure 5.1. Applied Load vs. Lateral Deflection for IPE 120 Profile with Span of 4.0 m. ....	30
Figure 5.2. Applied Load vs. Lateral Deflection for IPE 160 Profile with Span of 4.0 m. ....	30
Figure 5.3. Applied Load vs. Lateral Deflection for IPE 200 Profile with Span of 4.0 m. ....	31
Figure 5.4. Applied Load vs. Lateral Deflection for IPE 240 Profile with Span of 4.0 m. ....	31
Figure 5.5. Applied Load vs. Lateral Deflection for IPE 270 Profile with Span of 4.0 m. ....	32
Figure 5.6. Applied Load vs. Lateral Deflection for IPE 300 Profile with Span of 4.0 m. ....	32
Figure 5.7. Applied Load vs. Torsional Twist for IPE 120 Profile with Span of 4.0 m.....	34
Figure 5.8. Applied Load vs. Torsional Twist for IPE 160 Profile with Span of 4.0 m.....	34
Figure 5.9. Applied Load vs. Torsional Twist for IPE 200 Profile with Span of 4.0 m.....	35
Figure 5.10. Applied Load vs. Torsional Twist for IPE 240 Profile with Span of 4.0 m. ....	35
Figure 5.11. Applied Load vs. Torsional Twist for IPE 270 Profile with Span of 4.0 m. ....	36
Figure 5.12. Applied Load vs. Torsional Twist for IPE 300 Profile with Span of 4.0 m. ....	36
Figure 5.13. Applied Load vs. Vertical Deflection for IPE 120 Profile with Span of 4.0 m.....	38
Figure 5.14. Applied Load vs. Vertical Deflection for IPE 160 Profile with Span of 4.0 m.....	38
Figure 5.15. Applied Load vs. Vertical Deflection for IPE 200 Profile with Span of 4.0 m.....	39
Figure 5.16. Applied Load vs. Vertical Deflection for IPE 240 Profile with Span of 4.0 m.....	39
Figure 5.17. Applied Load vs. Vertical Deflection for IPE 270 Profile with Span of 4.0 m.....	40
Figure 5.18. Applied Load vs. Vertical Deflection for IPE 300 Profile with Span of 4.0 m.....	40

Figure 5.19. Vertical vs. Lateral Deflection for IPE 120 Profile with Span of 4.0 m.....	42
Figure 5.20. Vertical vs. Lateral Deflection for IPE 160 Profile with Span of 4.0 m.....	42
Figure 5.21. Vertical vs. Lateral Deflection for IPE 200 Profile with Span of 4.0 m.....	43
Figure 5.22. Vertical vs. Lateral Deflection for IPE 240 Profile with Span of 4.0 m.....	43
Figure 5.23. Vertical vs. Lateral Deflection for IPE 270 Profile with Span of 4.0 m.....	44
Figure 5.24. Vertical vs. Lateral Deflection for IPE 300 Profile with Span of 4.0 m.....	44
Figure 5.25. Applied Load vs. Lateral Deflection for IPE 200 Profile with Span of 2.0 m.....	46
Figure 5.26. Applied Load vs. Lateral Deflection for IPE 200 Profile with Span of 3.0 m.....	47
Figure 5.27. Applied Load vs. Lateral Deflection for IPE 200 Profile with Span of 4.0 m.....	47
Figure 5.28. Applied Load vs. Lateral Deflection for IPE 200 Profile with Span of 5.0 m.....	48
Figure 5.29. Applied Load vs. Lateral Deflection for IPE 200 Profile with Span of 6.0 m.....	48
Figure 5.30. Applied Load vs. Torsional Twist for IPE 200 Profile with Span of 2.0 m.....	50
Figure 5.31. Applied Load vs. Torsional Twist for IPE 200 Profile with Span of 3.0 m.....	50
Figure 5.32. Applied Load vs. Torsional Twist for IPE 200 Profile with Span of 4.0 m.....	51
Figure 5.33. Applied Load vs. Torsional Twist for IPE 200 Profile with Span of 5.0 m.....	51
Figure 5.34. Applied Load vs. Torsional Twist for IPE 200 Profile with Span of 6.0 m.....	52
Figure 5.35. Applied Load vs. Vertical Deflection for IPE 200 Profile with Span of 2.0 m.....	53
Figure 5.36. Applied Load vs. Vertical Deflection for IPE 200 Profile with Span of 3.0 m.....	53
Figure 5.37. Applied Load vs. Vertical Deflection for IPE 200 Profile with Span of 4.0 m.....	54
Figure 5.38. Applied Load vs. Vertical Deflection for IPE 200 Profile with Span of 5.0 m.....	54
Figure 5.39. Applied Load vs. Vertical Deflection for IPE 200 Profile with Span of 6.0 m.....	55
Figure 5.40. Vertical vs. Lateral Deflection for IPE 200 Profile with Span of 2.0 m.....	56
Figure 5.41. Vertical vs. Lateral Deflection for IPE 200 Profile with Span of 3.0 m.....	56
Figure 5.42. Vertical vs. Lateral Deflection for IPE 200 Profile with Span of 4.0 m.....	57
Figure 5.43. Vertical vs. Lateral Deflection for IPE 200 Profile with Span of 5.0 m.....	57
Figure 5.44. Vertical vs. Lateral Deflection for IPE 200 Profile with Span of 6.0 m.....	58

## **LIST OF TABLES**

Table 5.1. Values of C <sub>1</sub> and C <sub>2</sub> for transverse loading cases. (Bureau, 2005).....	20
Table 5.2. Critical buckling loads of different IPE profiles for 4 m beam span.....	25
Table 5.3. Critical buckling loads of IPE 200 profile beams of various spans.....	27
Table 5.4. Coefficient, a, of different IPE sections for 4.0 m beam span.....	28
Table 5.5. Coefficient, a, for IPE 200 profile beams of various spans.....	28



## LIST OF SYMBOLS

$\Pi$	= Potential Energy
$k_u$	= Lateral Stiffness
$k_v$	= Vertical Stiffness
$k_\phi$	= Torsional Stiffness
$v$	= Lateral Deflection
$v$	= Vertical Deflection
$\Phi$	= Rotational Twist
$E$	= Young's Modulus
$G$	= Shear Modulus
$I_z$	= Moment of Inertia About Major Axis
$I_y$	= Moment of Inertia About Minor Axis
$I_t$	= Torsional Constant
$I_w$	= Warping Constant
$M_{cr}$	= Elastic Critical Moment
$P$	= Point Load
$L$	= Unbraced Length of Beam
$\kappa$	= Effective Length Factor Referring to End Rotation

$k_w$	= Effective Length Factor Referring to End Warping
$\tilde{z}$	= Vertical Distance Between Point of Load Application and Shear Center
$C_1$	= Coefficient Depending on Loading Conditions
$C_2$	= Coefficient Depending on End Restraint Conditions
$b$	= Height of Cross-section
$C$	= Centroid of Cross-section Before Deformation
$C'$	= Centroid of Cross-section After Deformation
$y_b$	= Distance between Center of Rotation and Bottom of Beam Before Deformation
$y'_b$	= Distance between Center of Rotation and Bottom of Beam After Deformation

# 1. INTRODUCTION

## 1.1 BACKGROUND

Steel beams, especially European rolled I-sections (IPE sections), are by far the most widely used in the steel construction industry for buildings, bridges, and other structures. While these beams are effective in resisting bending about their major axis (vertical displacement), they are exposed to lateral instability. A beam which is loaded and bent in the plane of greatest flexural rigidity may buckle laterally (about minor axis) at a certain critical value of the load. This lateral buckling is of importance in the design of beams without lateral support, provided the flexural rigidity of the beam in the plane of bending is large in comparison with the lateral bending and torsional rigidity. If the load on such a beam is below the critical value, the beam will be stable in the upright position. As the load is increased, however, a condition is reached at which a slightly deflected and twisted form of equilibrium becomes possible, shown in Figure 1.1. The plane configuration of the beam is now unstable, and the lowest load at which this critical condition occurs represents the critical load for the beam. (Nseir, 2023; Timoshenko & Gere, 2012)

This global instability mode, shown in Figure 1.1, that affects slender, laterally unrestrained beams subjected to loads that cause deformations involving lateral deflection coupled with twisting of cross-section of the beam is called Lateral-torsional buckling (LTB). This mode governs the design of the beams when the unrestrained length is large compared with the torsional stiffness of the cross-section. (Trahair, 1993)

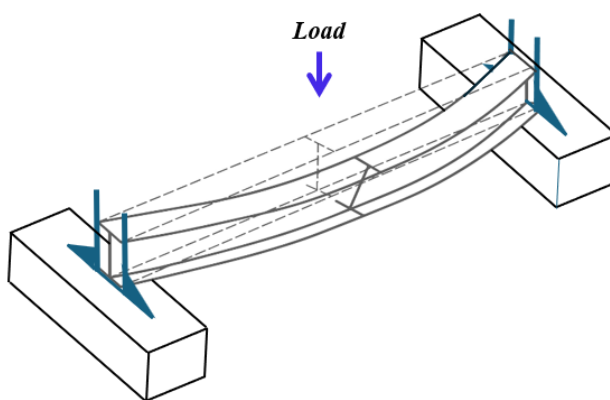


Figure 1.1. LTB of a simply-supported I-beam.

Extensive analytical, numerical, and experimental investigations about LTB have been conducted in the past. While numerical and experimental investigations have provided insights into the post-buckling response of steel beams, the use of analytical approaches have been limited upto the bifurcation point.

The present study aims to assess the post-buckling response behavior of simply-supported steel beams subjected to a midspan point load using simplified analytical approach. It deals specifically with IPE beams exhibiting “fork-type” end supports and ignoring the effect of warping.

## 1.2 MOTIVATION

In this thesis, the post-LTB response and the critical buckling load of a simply-supported IPE beam subjected to a midspan point load is explored using analytical methods applying the principle of minimum potential energy for assumed deformation path. Analytical and numerical approaches are used to estimate the beam’s response under the applied loading condition.

The objectives of this thesis are:

- To derive an approximate closed-form analytical solution for the post-buckling response using an assumed deformation path,
- To compare the analytical predictions with numerical solutions from OpenSeesPy,
- To identify the influence of section size and span length on the response.

The study aims to assess the benefits and limitations of the analytical approach in predicting the critical buckling load and post-buckling behavior by comparing the LTB responses with the results from the numerical method, thereby evaluating its applicability to practical purposes.

## 1.3 PROBLEM STATEMENT

This study is limited to simply-supported steel I beams, with a fork-type support inhibiting twist of cross-section at the ends as shown in Figure 1.1, subjected to a point load applied at midspan. The simply-supported beams are analysed using three approaches:

- i) Two analytical approaches by means of the principle of minimum potential energy, and
- ii) Numerical finite element model (FEM) approach using OpenSeesPy.

Furthermore, recommended formula from Eurocode is used for computation and comparison of critical buckling loads.

The beams are assumed to be made of linear elastic material, meaning no material nonlinearity is considered. The modelling assumed no cross-section warping. In addition, the analytical solutions use simplifying kinematic assumptions to permit closed-form results.

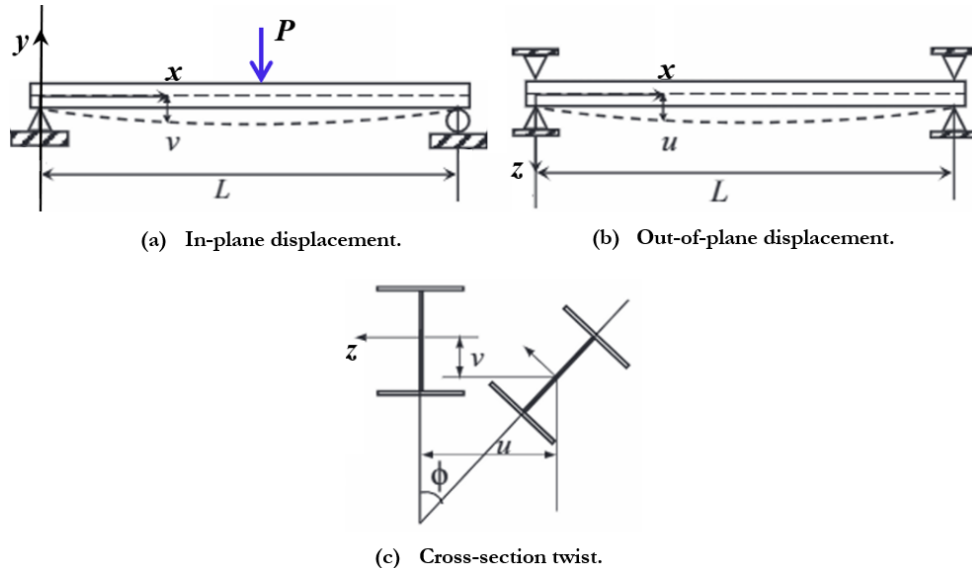


Figure 1.2. Deformation of a simply-supported I-beam subjected to point load.

#### 1.4 OUTLINE OF THE THESIS

This thesis is organized into six chapters, followed by references and appendices. A brief description of the content of each chapter is provided below:

Chapter 1: Introduction.

Chapter 2: Literature Review: - This chapter provides a focused review of previous studies related to post-buckling response in beams and research papers that are like this work. It discusses key findings and limitations of earlier works together with the methods that have been used in the field. The review helps to identify gaps and paves the way for the current study.

Chapter 3: Analytical Methodology: - This chapter presents the two deformation path assumptions with their theoretical background and how they are applied to find closed-form expressions for the LTB in simply-supported beams with the given boundary conditions.

Chapter 4: Numerical Methodology: - This chapter describes the numerical approach used for simulating the behavior of the simply-supported beams undergoing LTB using OpenSeesPy. It provides an overview of the FEM, material properties, boundary conditions, and the steps taken to simulate post-buckling behavior.

Chapter 5: Results and Discussion: - This chapter presents the results obtained from both the analytical and numerical methods. Computation and comparison of the critical buckling load and post-buckling behavior of beams with different cross-sections and spans are considered. The critical buckling loads are computed using three methods (Eurocode formulation, numerical approach and analytical method based on circular deformation path) and the comparison of post-buckling behaviors are shown using three methods (numerical approach and analytical methods based on circular and parabolic deformation paths).

Chapter 6: Conclusions and Recommendations for Future Work: - The final chapter summarizes the key findings of the study based on the analysis of the results. The conclusions drawn from the comparison of analytical and numerical methods are presented. Additionally, recommendations for future research directions, including potential improvements in modeling techniques, parameter consideration and areas requiring further investigation, are provided.

## **2.LITERATURE REVIEW**

### **2.1 INTRODUCTION**

LTB is particularly relevant in steel structures and is triggered when the applied major axis bending moment reaches a critical value, beyond which the beam can no longer maintain its original equilibrium configuration. (Timoshenko & Gere, 2012)

Different researchers have conducted numerical, analytical and experimental studies to show the LTB behavior of steel beams. This chapter presents a review of some of the studies.

### **2.2 ANALYTICAL STUDIES**

The classical closed-form solution for the elastic critical LTB capacity at the onset of buckling was first proposed by Timoshenko (1936) for simply supported, doubly symmetric, I-shaped members subjected to uniform moment through analytical study on the classical elastic buckling theory. This study was extended by Vlasov (1961) to account for warping torsion introducing St. Venant torsion and warping stiffnesses into the critical moment formulations. Although these formulations are the basis for design code provisions, they do not provide the post-buckling response of the beams beyond the bifurcation point. (Nayak et al., 2024; V. Z. Vlasov, 1961)

An investigation of the behavior of the buckled structure in the immediate neighborhood of the bifurcation point using theory of elastic stability analysis is performed by Koiter. (Koiter, 1945). The study used an asymptotic expansion of total potential energy leading to reduced amplitude equations with expansion coefficients that govern the stability of the nonlinear post-critical behavior. It showed the effect of geometric imperfections on the load capacity depending on the values and signs of the expansion coefficients.

### **2.3 DESIGN CODE RECOMMENDATION**

Eurocode 3 (*EN 1993-1-1*, 2005) provides widely used design formulas for elastic critical moment  $M_{cr}$ , incorporating flexural stiffness, torsional rigidity, and warping effects with effective length factors ( $C_1, C_2$ ).

In the NCCI technical reference (Bureau, 2005), a formula is presented for calculating the elastic critical LTB moment  $M_{cr}$ , derived from classical buckling theory, for a prismatic

beam members with doubly symmetric cross-section, loading in the plane of the web at which LTB occurs and taking into consideration the member's geometry, support conditions, and loading configuration with the following expression:

$$M_{cr} = C_1 \frac{\pi^2 EI_y}{(kL)^2} \left\{ \sqrt{\left(\frac{k}{k_w}\right)^2 \frac{I_w}{I_y} + \frac{(kL)^2 GI_t}{\pi^2 EI_y}} + (C_2 z_g)^2 - C_2 z_g \right\} \quad (2.1)$$

The expression in Equation 2.1 from the NCCI technical reference (Bureau, 2005) accounts for the coupled interaction of lateral displacement, torsional rotation, and warping resistance. The parameters  $C_1$  and  $C_2$ , which are typically obtained from tables, significantly influence the calculated value of  $M_{cr}$  and their values depend on loading conditions, end restraint conditions, and the shape of the bending moment diagram.

While Eurocode 3 offers guideline for determining the onset of LTB by primarily addressing the elastic critical moment, it does not provide guidance on the post-buckling behavior of beams.

#### 2.4 MODIFICATION FACTORS

Analytical expressions for the critical load have been modified to capture more complex scenarios. One example is the study by Andarde (2007). In the study the domain of application of the commonly employed "three-factor formula" to estimate the elastic critical moment of steel beams prone to LTB was extended to I-section cantilevers. The study considered cantilever I-section beams (i) with equal or unequal flanges, (ii) fully built-in or free to warp at the support and (iii) acted on by uniformly distributed or concentrated tip loads (applied either at the shear centre or at one of the flanges). It used numerical results of a parametric study, obtained by the Rayleigh–Ritz method, for the development of approximate analytical expressions for the  $C_1$ ,  $C_2$  and  $C_3$  factors appearing in the three-factor formula shown in Equation 2.2. (Andrade et al., 2007)

$$M_{cr} = C_1 \frac{\pi^2 EI_y}{(kL)^2} \left\{ \sqrt{\left(\frac{k}{k_w}\right)^2 \frac{I_w}{I_y} + \frac{(kL)^2 GI_t}{\pi^2 EI_y}} + (C_2 z_g - C_3 z_j)^2 - (C_2 z_g - C_3 z_j) \right\} \quad (2.2)$$

A second example is the study by Nayak (2024) that investigated the suitability of commonly used LTB modification factors in literature and design specifications under varying moment gradients and boundary conditions, accomplished via comparisons with analytical solutions using the Rayleigh-Ritz method and numerical solutions from finite element analyses. In the study analytical LTB modification factors are derived for doubly symmetric I-shaped members with different combinations of ideal flexural and torsional boundary conditions (simply supported and fixed) and subjected to different loading

scenarios. The validity of the modification factors is also assessed for intermediate restraint conditions. (Nayak et al., 2024)

## 2.5 EXPERIMENTAL AND NUMERICAL STUDIES

Both numerical simulations utilizing FEM and experimental testings have been utilized to investigate LTB, facilitating parametric studies and validations. A notable study on the behaviour of Steel I-Beams exhibiting LTB at elevated temperature has been carried out by comparison of experimental and numerical analysis by Vila Real (2003). A set of 120 full-scale tests based on a reaction frame and on a hydraulic system has been carried out for beams of IPE 100 sections with lengths varying from 0.5 to 6.5 m, submitted to temperatures varying from room temperature to 600 °C. The study proposed a safer model to predict the LTB resistance in fire design situation through validation. (Vila Real et al., 2003)

Gonçalves employed a two-node geometrically exact beam finite elements to assess the behaviour of steel I-section beams undergoing large displacements, finite rotations and LTB including post-buckling behaviour. The study examined three support/ loading cases, namely: simply supported beams under uniform moment, simply supported beams subjected to a midspan vertical force and cantilevers subjected to a free end vertical force, to determine (i) elastic nonlinear bifurcation loads (i.e., bifurcation loads accounting for pre-buckling deflections), (ii) large displacement elastic post-buckling paths including geometric imperfection effects and (iii) large displacement elastoplastic equilibrium paths accounting for geometric imperfections and residual stresses with a particular focus on both standard and wide-flange I-sections. (Gonçalves, 2019)

An analytical, numerical and experimental investigation on the LTB of hot-rolled steel I-section beams with fork-type end supports and acted by simple transverse loadings (mostly applied end moments) and various axial tension values is done by Nseir (2023). In the study derivation and validation of an analytical expression providing critical buckling moments of uniformly bent beams subjected to tension was presented. The analytical finding was followed by a numerical study on the beneficial influence of axial tension on beams under non-uniform bending. The paper addressed the performance of two experimental tests aimed at determining the behavior and ultimate strength of narrow and wide flange beams subjected to eccentric axial tension. (Nseir, 2023)



## 3.ANALYTICAL MODELING

### 3.1 STRUCTURAL MODELLING AND PROCEDURE

The analytical procedure developed in this study evaluates the LTB behavior of simply-supported steel I-section beams subjected to bending about their major axis due to a point load at midspan, shown in Figure 3.1. Classical beam theory and principle of minimum potential energy are used to find formulations capturing the coupled interaction between lateral displacement (minor axis deflection) and torsional rotation that characterizes LTB. The primary goal is to derive the load-displacement response, capturing both the critical buckling load and post-buckling behavior under increasing transverse point load at midspan. The analytical approach provides an understanding of the beam's stability response under idealized loading and support conditions. This response is used for comparison with the results of finite element simulations which are the benchmarks.

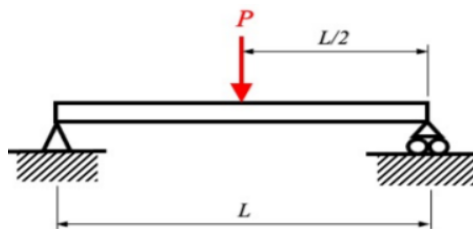


Figure 3.1. Simply-supported beam subjected to point load at midspan.

The beam is homogeneous, linearly elastic, and prismatic, with material properties corresponding to typical structural steel used in IPE sections. Young's modulus of  $E=200$  GPa and shear modulus of  $G=80$  GPa are taken, which are treated as constants throughout the analysis, assuming isotropic behavior and neglecting material nonlinearity or plasticity effects.

Geometric properties of the beam section are obtained from standard European IPE profiles, including the height  $h$ , cross-sectional area  $A$ , minor and major axis moments of inertia  $I_y$  and  $I_z$ , torsional constant  $I_t$ , and warping constant  $I_w$ . The profiles of the beam considered in this study are from IPE 120 to IPE 300 with unbraced span lengths varying from 2.0 m to 6.0 m. The beam is assumed to be simply-supported at both ends with lateral and torsional restraints provided by fork-type supports.

The analytical model assumes circular and parabolic deformation paths for the relationship between vertical and lateral displacement. The midspan twist angle serves as a parametric variable to describe the deformed shape taking into consideration torsional rotation. The corresponding flexural stiffness about the strong axis is defined as  $k_v$ , flexural stiffness about the weak axis is defined as  $k_u$ , and the torsional stiffness is given by  $k_\phi$ . Derivation of expressions for the stiffnesses that govern the resistance of the beam to vertical, lateral and torsional deformations are shown in section 3.2. Although the stiffness terms change with deformations, constant values of stiffnesses are used in this thesis work.

Using the principle of minimum potential energy, the equilibrium path is derived by first finding the total potential energy from internal strain energy and the external work done by the applied transverse point load followed by minimizing the total potential energy with respect to the lateral displacement  $u$  and torsional rotation (twist angle)  $\phi$ , as shown in Figure 1.2. This leads to a nonlinear equation involving trigonometric functions and their interaction with geometric and material properties which provides an expression for the applied point load  $P$ , shown in Figure 3.1, as a function of the twist angle, stiffnesses and other system parameters, capturing the full behavior including the buckling and post-buckling response of the beam at the midspan.

### 3.2 DISCRETIZATION

To permit closed-form analytical modeling, the beam is approximated using a discrete system. The force-deformation in the major and minor axes, and the twist are modeled as discrete degrees of freedom with associated stiffnesses. The degrees of freedom assume "modal" deformations associated with the deformations caused by a midspan point load. The simply-supported beam subjected to a point load at midspan is modelled as a beam with vertical and lateral linear springs at the midspan and torsional springs at the supports.

#### 3.2.1 Vertical Stiffness

A vertical load  $P$  is applied at midspan on the simply-supported beam system as shown in Figure 3.2.

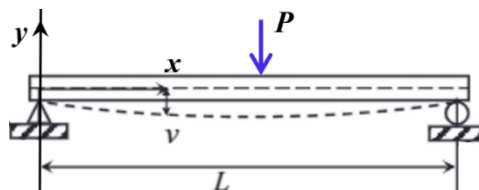


Figure 3.2. Vertical deflection of simply-supported beam due to vertical point load.

The vertical displacement  $v$  at midspan due to the applied vertical load  $P$  is:

$$v = \frac{PL^3}{48EI_z} \quad (3.1)$$

Then, the vertical load causing the vertical displacement  $v$  at midspan is:

$$P = \frac{48EI_z}{L^3} v \quad (3.2)$$

The vertical stiffness is the force required to cause a unit vertical displacement  $v$ . Therefore, the vertical stiffness of the system is:

$$k_v = \frac{48EI_z}{L^3} \quad (3.3)$$

### 3.2.2 Lateral Stiffness

The lateral stiffness is equal to a lateral force required to cause a unit lateral displacement. It is derived in a similar way as the vertical stiffness, and it involves the minor axis moment of inertia. Therefore, the lateral stiffness of the system is:

$$k_u = \frac{48EI_y}{L^3} \quad (3.4)$$

### 3.2.3 Torsional Stiffness

A torsional moment  $T$  is applied at midspan on the simply-supported beam system as shown in Figure 3.3.

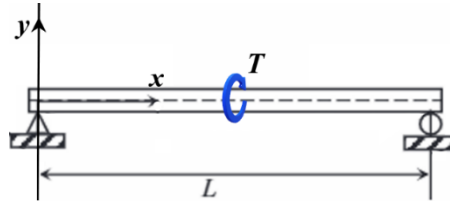


Figure 3.3. Twist of simply-supported beam due to torsional moment.

The expression for the angle of twist  $\phi$  at midspan due to the applied torsional moment  $T$  is derived as:

$$\frac{d\phi}{dx} = \frac{T}{GI_t} \quad (3.5)$$

$$d\phi = \frac{T}{GI_t} dx \quad (3.6)$$

Integrating both sides of Equation 3.6:

$$\phi = \int_0^{L/2} \frac{T/2}{GI_t} dx \quad (3.7)$$

$$\phi = \frac{(T/2)}{GI_t} \left( \frac{L}{2} \right) \quad (3.8)$$

Then, the torsional moment causing the torsional rotation  $\phi$  at midspan is:

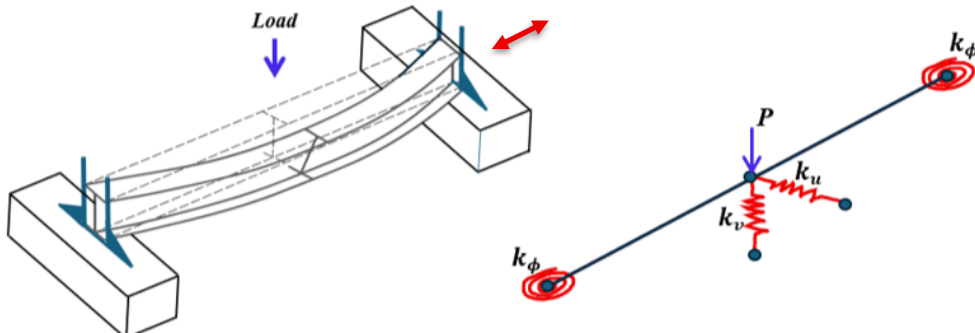
$$T = \frac{4GI_t}{L} \phi \quad (3.9)$$

The torsional stiffness is the torsional moment required to cause a unit torsional rotation  $\phi$ . Therefore, the torsional stiffness of the system is:

$$k_\phi = \frac{4GI_t}{L} \quad (3.10)$$

### 3.3 GENERAL POTENTIAL ENERGY EQUATION

The potential energy for the simply-supported beam subjected to midspan point load  $P$  shown in Figure 3.4(a) and that is modelled as a beam with torsional springs with stiffness of  $k_\phi$  at the supports, a lateral linear spring with stiffness of  $k_u$  and a vertical linear spring with stiffness of  $k_v$  at the midspan shown in Figure 3.4(b) is given in Equation 3.11.



(a) Simply-supported beam.

(b) Discretization model of the beam.

Figure 3.4. Discretization of simply-supported beam subjected to point load.

$$\Pi = \left[ \frac{1}{2} k_u u^2 \right] + 2 * \left[ \frac{1}{2} k_\phi \phi^2 \right] - [Pv] \quad (3.11)$$

- The first term,  $\left[\frac{1}{2}k_u u^2\right]$ , is the potential energy due to the lateral deflection.
- The second term,  $\left[\frac{1}{2}k_\phi \phi^2\right]$ , is the potential energy related to the twisting of the section about its longitudinal axis. It is multiplied by two because of the two rotational springs at the two ends of the beam.
- The third term,  $-[Pv]$ , is the potential energy lost through the vertical motion of the point load.

The vertical load  $P$  is assumed to be applied at the centroid of the section, and the beam is pinned at one end and free to move longitudinally at the other end as shown with the bi-directional red arrow in Figure 3.4(a).

The relationship of the lateral displacement  $u$  and vertical displacement  $v$  of the centroid of the section, shown in Figure 3.5, depends on the chosen deformation path. In general, these are two independent degrees of freedom. However, two alternative kinematic assumptions are used here to simplify the analysis. In Sections 3.4 and 3.5 expressions showing their relationship are derived for circular and parabolic deformation paths respectively, shown in Figure 3.5.

Note that in Figure 3.5 all variables, points, lines, shapes and variables in blue are for circular path, while the ones in red are for parabolic path and the ones in black are used in both cases.

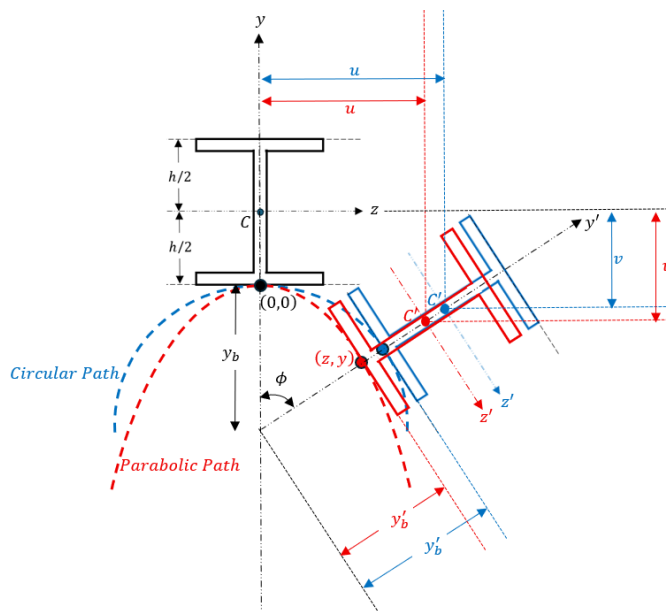


Figure 3.5. Assumed deformed orientation of the cross-section for the two paths.

### 3.4 CIRCULAR DEFORMATION PATH

In this section the beam is assumed to follow a circular deformation path, represented by the blue broken curve in Figure 3.5, after lateral instability. The undeformed orientation of the cross-section of the beam is shown in black while the deformed orientation is shown in blue in Figure 3.5 above.

From the figure, using trigonometric relations and linear vertical deflection equation, the lateral displacement  $u$  and the vertical displacement  $v$  of the centroid of the section are:

$$u = \left( y'_b + \frac{h}{2} \right) \sin\phi \quad (3.12)$$

$$v = \frac{P}{k_v} - \left( y'_b + \frac{h}{2} \right) \cos\phi + \left( y_b + \frac{h}{2} \right) \quad (3.13)$$

In the above expression for the vertical deflection, the first term is related to the dependency of the vertical displacement on the applied point load and the vertical stiffness of the beam. This term does not vanish unless the applied load becomes zero or the vertical stiffness is very large. The remaining two terms in Equation 3.13 and the expression for the lateral displacement in Equation 3.12 are found by applying trigonometry to the deformed and undeformed orientation of the beam cross-section after lateral instability shown in Figure 3.5.

Assuming a circular path of deflection (i.e. The curve showing the deflection-path is assumed to be a circle with radius of  $y_b = y'_b$ ).

Rearranging the lateral displacement expression in Equation 3.12:

$$\begin{aligned} u &= \left( y_b + \frac{h}{2} \right) \sin\phi \\ \Rightarrow y_b + \frac{h}{2} &= \frac{u}{\sin\phi} \end{aligned} \quad (3.14)$$

From the vertical displacement expression in Equation 3.13:

$$\begin{aligned} v &= \frac{P}{k_v} - \left( y_b + \frac{h}{2} \right) \cos\phi + \left( y_b + \frac{h}{2} \right) \\ \Rightarrow v &= \frac{P}{k_v} + \left( y_b + \frac{h}{2} \right) (1 - \cos\phi) \end{aligned} \quad (3.15)$$

Substituting the expression from Equation 3.14 into Equation 3.15, the vertical displacement  $v$  of the centroid of the section will be:

$$\Rightarrow v = \frac{P}{k_v} + \left( \frac{u}{\sin\phi} \right) (1 - \cos\phi)$$

$$\Rightarrow v = \frac{P}{k_v} + u \left( \frac{1 - \cos\phi}{\sin\phi} \right) \quad (3.16)$$

Substituting the above expression into the total potential energy formulation shown in Equation 3.11:

$$\begin{aligned} \Pi &= \left[ \frac{1}{2} k_u u^2 \right] + 2 * \left[ \frac{1}{2} k_\phi \phi^2 \right] - [Pv] \\ \Rightarrow \Pi &= \left[ \frac{1}{2} k_u u^2 \right] + 2 * \left[ \frac{1}{2} k_\phi \phi^2 \right] - \left[ P * \left( \frac{P}{k_v} + u \left( \frac{1 - \cos\phi}{\sin\phi} \right) \right) \right] \\ \Rightarrow \Pi &= \frac{1}{2} k_u u^2 + k_\phi \phi^2 - Pu \left( \frac{1 - \cos\phi}{\sin\phi} \right) - \frac{P^2}{k_v} \end{aligned} \quad (3.17)$$

### 3.4.1 Minimization of Potential Energy

The minimization of the potential energy is done with respect to the lateral displacement  $u$  and rotational twist  $\phi$  to find the equilibrium path.

$$\frac{\partial \Pi}{\partial u} = 0 \Rightarrow \frac{\partial}{\partial u} \left( \frac{1}{2} k_u u^2 + k_\phi \phi^2 - Pu \left( \frac{1 - \cos\phi}{\sin\phi} \right) - \frac{P^2}{k_v} \right) = 0 \quad (3.18)$$

$$\Rightarrow k_u u - P \left( \frac{1 - \cos\phi}{\sin\phi} \right) = 0 \quad (3.19)$$

$$\Rightarrow P = k_u u \left( \frac{\sin\phi}{1 - \cos\phi} \right) \quad (3.20)$$

$$\frac{\partial \Pi}{\partial \phi} = 0 \Rightarrow \frac{\partial}{\partial \phi} \left( \frac{1}{2} k_u u^2 + k_\phi \phi^2 - Pu \left( \frac{1 - \cos\phi}{\sin\phi} \right) - \frac{P^2}{k_v} \right) = 0 \quad (3.21)$$

$$\Rightarrow 2k_\phi \phi - Pu \left( \frac{\sin^2\phi - \cos\phi(1 - \cos\phi)}{\sin^2\phi} \right) = 0$$

$$\Rightarrow 2k_\phi \phi - Pu \left( \frac{\sin^2\phi + \cos^2\phi - \cos\phi}{\sin^2\phi} \right) = 0$$

$$\Rightarrow 2k_\phi \phi - Pu \left( \frac{1 - \cos\phi}{\sin^2\phi} \right) = 0$$

$$\Rightarrow 2k_\phi \phi - Pu \left( \frac{1 - \cos\phi}{1 - \cos^2\phi} \right) = 0$$

$$\Rightarrow 2k_\phi \phi - Pu \left( \frac{1}{1 + \cos\phi} \right) = 0 \quad (3.22)$$

$$\Rightarrow P = \frac{2k_\phi \phi}{u} (1 + \cos\phi) \quad (3.23)$$

### 3.4.2 Equilibrium Path

Equating Equations 3.20 and 3.23:

$$\begin{aligned} k_u u \left( \frac{\sin\phi}{1 - \cos\phi} \right) &= \frac{2k_\phi\phi}{u} (1 + \cos\phi) \\ u^2 &= \frac{2k_\phi\phi}{k_u} \left( \frac{1 - \cos^2\phi}{\sin\phi} \right) = \frac{2k_\phi\phi}{k_u} \left( \frac{\sin^2\phi}{\sin\phi} \right) \\ u^2 &= \frac{2k_\phi}{k_u} (\phi \sin\phi) \end{aligned} \quad (3.24)$$

From Equation 3.20:

$$\begin{aligned} P &= k_u u \left( \frac{\sin\phi}{1 - \cos\phi} \right) \\ u &= \frac{P}{k_u} \left( \frac{1 - \cos\phi}{\sin\phi} \right) \end{aligned} \quad (3.25)$$

Substituting the above expression into Equation 3.24:

$$\begin{aligned} \left[ \frac{P}{k_u} \left( \frac{1 - \cos\phi}{\sin\phi} \right) \right]^2 &= \frac{2k_\phi}{k_u} (\phi \sin\phi) \\ \frac{P^2}{k_u^2} \left( \frac{(1 - \cos\phi)^2}{\sin^2\phi} \right) &= \frac{2k_\phi}{k_u} (\phi \sin\phi) \\ \frac{P^2}{k_u} \left( \frac{1 - \cos\phi}{1 + \cos\phi} \right) &= 2k_\phi (\phi \sin\phi) \\ P^2 &= 2k_\phi k_u \left( (\phi \sin\phi) \left( \frac{1 + \cos\phi}{1 - \cos\phi} \right) \right) \\ P^2 &= 2k_\phi k_u \left( (\phi \sin\phi) \left( \frac{(1 + \cos\phi)^2}{1 - \cos^2\phi} \right) \right) = 2k_\phi k_u \left( (\phi \sin\phi) \left( \frac{(1 + \cos\phi)^2}{\sin^2\phi} \right) \right) \\ P^2 &= 2k_\phi k_u \left( \phi \frac{(1 + \cos\phi)^2}{\sin\phi} \right) \\ P &= \sqrt{2k_\phi k_u \left( \phi \frac{(1 + \cos\phi)^2}{\sin\phi} \right)} \end{aligned} \quad (3.26)$$

The equilibrium path for the assumed circular deformation path is a function of two stiffness parameters and the twist angle at midspan of the beam as shown in Equation 3.26.

### 3.5 PARABOLIC DEFORMATION PATH

In this section the beam is assumed to follow a parabolic deformation path, represented by the red broken curve in Figure 3.5, after lateral instability. The undeformed orientation of the cross-section of the beam is shown in black while the deformed orientation is shown in red in Figure 3.5 above.

Applying trigonometric relations and linear vertical deflection equation, the lateral displacement  $u$  and the vertical displacement  $v$  of the centroid of the section are:

$$u = \left( y'_b + \frac{h}{2} \right) \sin\phi \quad (3.27)$$

$$v = \frac{P}{k_v} - \left( y'_b + \frac{h}{2} \right) \cos\phi + \left( y_b + \frac{h}{2} \right) \quad (3.28)$$

Assuming a parabolic path of deflection with the following expression:

$$y = a \cdot z^2 + b \cdot z + c \quad (3.29)$$

Where:  $a$ ,  $b$  and  $c$  are coefficients of the parabolic path of deflection and taking the origin as shown in Figure 3.5. The coefficients  $b$  and  $c$  are zero as shown in Appendix A. Therefore, the equation of the parabola is:

$$\Rightarrow y = a \cdot z^2 \quad (3.30)$$

The value of  $a$  should be chosen in such a way that the parabolic solution gives better prediction of the responses of the beam and this is shown in Section 5.2.

Considering the bottom of the deflected beam cross-section along its axis of symmetry inclined at an angle of  $\phi$  as the second point on the deflection-path with coordinate  $(z, y)$  and applying trigonometry to find  $z$  and  $y$ :

$$z = u - \frac{h}{2} \sin\phi \quad (3.31)$$

$$y = y_b - y'_b \cos\phi \quad (3.32)$$

The vertical displacement in Equation 3.28 is expanded as:

$$\begin{aligned} v &= \frac{P}{k_v} - \left( y'_b + \frac{h}{2} \right) \cos\phi + \left( y_b + \frac{h}{2} \right) \\ v &= \frac{P}{k_v} - y'_b \cos\phi + y_b - \frac{h}{2} \cos\phi + \frac{h}{2} \end{aligned} \quad (3.33)$$

Combining Equations 3.32 and 3.33 then solving for  $y$ :

$$v = \frac{P}{k_v} + y - \frac{h}{2} \cos\phi + \frac{h}{2} \quad (3.34)$$

$$y = v - \frac{P}{k_v} - \frac{h}{2} + \frac{h}{2} \cos\phi \quad (3.35)$$

Therefore, the coordinate of the second point on the deflection-path becomes:

$$(x, y) = \left( u - \frac{h}{2} \sin\phi, v - \frac{P}{k_v} - \frac{h}{2} + \frac{h}{2} \cos\phi \right) \quad (3.36)$$

Solving the deflection-path equation, shown in Equation 3.30, at the second point:

$$\begin{aligned} y &= a \cdot z^2 \\ v - \frac{P}{k_v} - \frac{h}{2} + \frac{h}{2} \cos\phi &= a \cdot \left( u - \frac{h}{2} \sin\phi \right)^2 \\ \Rightarrow v &= a \cdot \left( u - \frac{h}{2} \sin\phi \right)^2 - \frac{h}{2} \cos\phi + \frac{h}{2} + \frac{P}{k_v} \\ \Rightarrow v &= a \cdot \left( u - \frac{h}{2} \sin\phi \right)^2 + \frac{h}{2} (1 - \cos\phi) + \frac{P}{k_v} \end{aligned} \quad (3.37)$$

Substituting the above expression of  $v$  into the total potential energy formulation shown in Equation 3.11:

$$\begin{aligned} \Pi &= \left[ \frac{1}{2} k_u u^2 \right] + 2 * \left[ \frac{1}{2} k_\phi \phi^2 \right] - [Pv] \\ \Rightarrow \Pi &= \left[ \frac{1}{2} k_u u^2 \right] + 2 * \left[ \frac{1}{2} k_\phi \phi^2 \right] - \left[ P * \left( a \cdot \left( u - \frac{h}{2} \sin\phi \right)^2 + \frac{h}{2} (1 - \cos\phi) + \frac{P}{k_v} \right) \right] \\ \Rightarrow \Pi &= \frac{1}{2} k_u u^2 + k_\phi \phi^2 - P * \left( a \cdot \left( u - \frac{h}{2} \sin\phi \right)^2 + \frac{h}{2} (1 - \cos\phi) + \frac{P}{k_v} \right) \end{aligned} \quad (3.38)$$

### 3.5.1 Minimization of Potential Energy

As shown in Equation 3.38, the potential energy, in addition to other parameters, is a function of two displacement variables  $u$  and  $\phi$ . Therefore, minimization of the potential energy is done with respect to the lateral displacement  $u$  and the rotational twist  $\phi$  to find the equilibrium path.

$$\begin{aligned} \frac{\partial \Pi}{\partial u} = 0 &\Rightarrow \frac{\partial}{\partial u} \left( \frac{1}{2} k_u u^2 + k_\phi \phi^2 - P \left( a \left( u - \frac{h}{2} \sin\phi \right)^2 + \frac{h}{2} (1 - \cos\phi) + \frac{P}{k_v} \right) \right) = 0 \\ &\Rightarrow k_u u - 2P * a \left( u - \frac{h}{2} \sin\phi \right) = 0 \end{aligned} \quad (3.39)$$

$$\Rightarrow P = \frac{k_u u}{2a \left( u - \frac{h}{2} \sin\phi \right)} \quad (3.40)$$

$$\begin{aligned}
\frac{\partial \Pi}{\partial \phi} = 0 &\Rightarrow \frac{\partial}{\partial \phi} \left( \frac{1}{2} k_u u^2 + k_\phi \phi^2 - P \left( a \left( u - \frac{h}{2} \sin \phi \right)^2 + \frac{h}{2} (1 - \cos \phi) + \frac{P}{k_v} \right) \right) = 0 \\
&\Rightarrow 2k_\phi \phi - P * \left( 2a \cdot \left( u - \frac{h}{2} \sin \phi \right) \cdot \left( -\frac{h}{2} \cos \phi \right) + \frac{h}{2} (\sin \phi) \right) = 0 \\
&\Rightarrow 2k_\phi \phi - P * \left( a \cdot h \cdot \cos \phi \left( \frac{h}{2} \sin \phi - u \right) + \frac{h}{2} (\sin \phi) \right) = 0 \\
&\Rightarrow 2k_\phi \phi - P * \frac{h}{2} \left( a \cdot h \cdot \cos \phi \left( \sin \phi - \frac{2u}{h} \right) + \sin \phi \right) = 0 \\
&\Rightarrow 4k_\phi \phi - P * h \left( a \cdot h \cdot \cos \phi \left( \sin \phi - \frac{2u}{h} \right) + \sin \phi \right) = 0 \tag{3.41}
\end{aligned}$$

$$\Rightarrow P = \frac{4k_\phi \phi}{h \left( a \cdot h \cdot \cos \phi \left( \sin \phi - \frac{2u}{h} \right) + \sin \phi \right)} \tag{3.42}$$

### 3.5.2 Equilibrium Path

Solving for  $u$  from Equation 3.39:

$$\begin{aligned}
k_u u - 2P \cdot a \left( u - \frac{h}{2} \sin \phi \right) &= 0 \\
k_u u - 2P \cdot a \cdot u + P \cdot a \cdot h \cdot \sin \phi &= 0 \\
k_u u - 2P \cdot a \cdot u &= -P \cdot a \cdot h \cdot \sin \phi \\
u &= \frac{P \cdot a \cdot h \cdot \sin \phi}{2P \cdot a - k_u} \tag{3.43}
\end{aligned}$$

Expanding Equation 3.41 and substituting the expression of  $u$  from Equation 3.43:

$$\begin{aligned}
4k_\phi \phi - P \cdot h \left( a \cdot h \cdot \cos \phi \left( \sin \phi - \frac{2u}{h} \right) + \sin \phi \right) &= 0 \\
4k_\phi \phi - P \cdot h (a \cdot h \cdot \cos \phi \sin \phi - a \cdot \cos \phi \cdot 2u + \sin \phi) &= 0 \\
4k_\phi \phi - P \cdot h \left( a \cdot h \cdot \cos \phi \sin \phi - a \cdot \cos \phi \cdot 2 \left( \frac{P \cdot a \cdot h \cdot \sin \phi}{2P \cdot a - k_u} \right) + \sin \phi \right) &= 0 \\
4k_\phi \phi - P \cdot h \left( \frac{(2P \cdot a^2 \cdot h \cdot \cos \phi \sin \phi - k_u \cdot a \cdot h \cdot \cos \phi \sin \phi - 2P \cdot a^2 \cdot h \cdot \cos \phi \sin \phi) + sin \phi}{2P \cdot a - k_u} \right) &= 0 \\
4k_\phi \phi - P \cdot h \left( \frac{-k_u \cdot a \cdot h \cdot \cos \phi \sin \phi + 2P \cdot a \cdot \sin \phi - k_u \sin \phi}{2P \cdot a - k_u} \right) &= 0
\end{aligned}$$

$$\frac{8Pk_{\phi}\phi \cdot a - 4\phi k_{\phi}k_u - P \cdot h(-k_u \cdot a \cdot h \cdot \cos\phi \sin\phi + 2P \cdot a \cdot \sin\phi - k_u \sin\phi)}{2P \cdot a - k_u} = 0$$

$$8Pk_{\phi}\phi \cdot a - 4\phi k_{\phi}k_u + P \cdot a \cdot h^2 \cdot k_u \cdot \cos\phi \sin\phi - 2P^2 \cdot a \cdot h \cdot \sin\phi + P \cdot h \cdot k_u \sin\phi = 0$$

$$P^2 \cdot (-2a \cdot h \cdot \sin\phi) + P \cdot (8a \cdot k_{\phi}\phi + a \cdot h^2 \cdot k_u \cdot \cos\phi \sin\phi + h \cdot k_u \sin\phi) - 4\phi k_{\phi}k_u = 0 \quad (3.44)$$

The above expression is a quadratic equation as a function of the applied load P which can be written as:

$$a_1 \cdot P^2 + b \cdot P + c = 0 \quad (3.45)$$

Where:

$$\left\{ \begin{array}{l} a_1 = -2a \cdot h \cdot \sin\phi \\ b = 8a \cdot k_{\phi}\phi + a \cdot h^2 \cdot k_u \cdot \cos\phi \sin\phi + h \cdot k_u \sin\phi \\ c = -4\phi k_{\phi}k_u \end{array} \right\} \quad (3.46)$$

Solving for P using the quadratic solution:

$$P = \frac{-b \pm \sqrt{b^2 - 4 * a_1 * c}}{2 * a_1}$$

The two solutions of P are  $P_1$  and  $P_2$  as shown in the following expressions:

$$P_1 = \frac{\frac{ah^2k_u \sin(2\phi)}{2} + 8ak_{\phi}\phi + hk_u \sin\phi - \sqrt{\frac{a^2h^4k_u^2(1 - \cos(4\phi))}{8} + 8a^2h^2k_{\phi}k_u \phi \sin(2\phi) + 64a^2k_{\phi}^2\phi^2 + 2ah^3k_u^2 \sin^2(\phi)\cos\phi - 16ahk_{\phi}k_u \phi \sin(\phi) + h^2k_u^2 \sin^2(\phi)}}{4ah \sin(\phi)} \quad (3.47)$$

$$P_2 = \frac{\frac{ah^2k_u \sin(2\phi)}{2} + 8ak_{\phi}\phi + hk_u \sin\phi + \sqrt{\frac{a^2h^4k_u^2(1 - \cos(4\phi))}{8} + 8a^2h^2k_{\phi}k_u \phi \sin(2\phi) + 64a^2k_{\phi}^2\phi^2 + 2ah^3k_u^2 \sin^2(\phi)\cos\phi - 16ahk_{\phi}k_u \phi \sin(\phi) + h^2k_u^2 \sin^2(\phi)}}{4ah \sin(\phi)} \quad (3.48)$$

The two expressions shown in Equations 3.47 and 3.48 representing the equilibrium paths for the assumed parabolic deformation path are more complex functions than the one found for the circular path in Equation 3.26. The equilibrium paths depend on two stiffness parameters, the twist angle at midspan, height of the section and coefficient of the parabolic path.

Depending on the direction of instability the two expressions give symmetric equilibrium paths. This is shown in the comparison of post-buckling response in Section 5.3.

## 4. NUMERICAL MODELING

### 4.1 STRUCTURAL MODELLING AND PROCEDURE

To simulate the LTB behavior of simply-supported steel I-beam subjected to point load at midspan, FEM was developed using OpenSeesPy, the Python interface for the OpenSees structural analysis framework. This simulation enables an investigation of instability behavior across a variety of beam geometries and serves as a numerical counterpart to the analytical LTB predictions.

The beam is modeled using three nodes and two elastic beam-column elements, as shown in Figure 4.1, which account for flexural stiffness about both principal axes and torsional rigidity. Node-1 corresponds to the pinned support, Node-3 to the roller support, and node-2 lies at midspan where a vertical point load is applied. To initiate buckling, a small initial imperfection is introduced in the lateral-direction at node-2. A corotational geometric transformation is utilized to capture large displacements and rotations, which are needed for simulating the nonlinear post-buckling behavior.

Assuming that buckling occurs prior to yielding, although this is not the case in all design scenarios, material behavior is modeled as linearly elastic. Steel is defined using an elastic uniaxial material with a modulus of elasticity  $E=200$  GPa and shear modulus  $G=80$  GPa, typical of structural steel. Since the focus of this study is on the elastic stability, no material inelasticity is considered. Section properties, including cross-sectional area, moments of inertia and torsional constant are assigned using elastic section definitions based on the selected IPE profile.

The boundary conditions are defined to realistically simulate simply-supported conditions with fork-type supports at the two ends while allowing lateral-torsional movement. Node-1 is fully restrained in all translational degrees of freedom and in rotation about the longitudinal-axis, but it is free to rotate about the major- and minor-axes. Node-3 is restrained in vertical and lateral translations and rotation about the longitudinal-axis, but it is free to translate in the longitudinal direction and free to rotate about the major- and minor-axes. These boundary conditions provided by the pin, roller and fork-type supports facilitate the full expression of LTB behavior without over-constraining the structure.

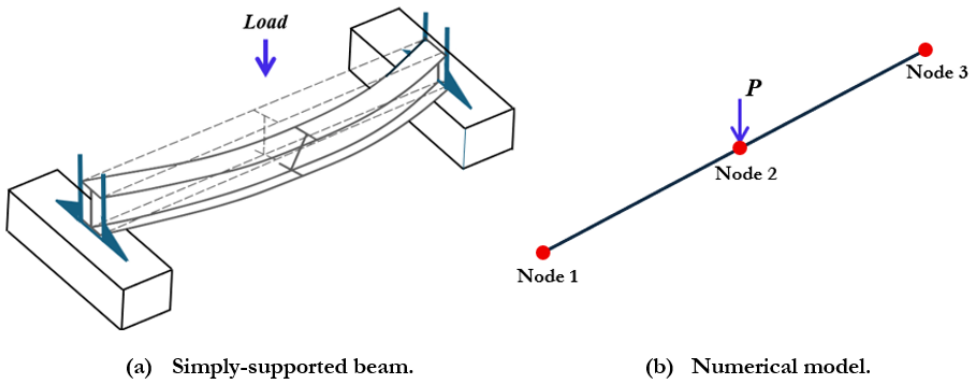


**Figure 4.1. Numerical model of simply-supported beam subjected to point load.**

A vertical point load is applied at the midspan node using a linear time series, and a static analysis is conducted using the arc-length control method. This approach allows the simulation to trace the response beyond the critical buckling load and capture post-buckling deformation. Throughout the analysis, structural responses including vertical deflection, lateral displacement, torsional rotation, and applied load factor are recorded at each increment. These are then visualized through automatically generated plots, such as load-deflection, load-twist and deformed shape curves, providing insight into the beam's stability performance under increasing load.

The OpenSeesPy code for the numerical analysis is shown in Appendix B.

## 5.RESULTS AND DISCUSSION

This section shows and compares the results, obtained for LTB analysis of simply-supported steel beams with IPE profiles, from numerical modeling and analytical solutions, assuming both circular and parabolic deformation paths. The following subsections provide a detailed comparison of these approaches:

### 5.1 COMPARISON OF CRITICAL BUCKLING LOAD

This section presents the comparative analysis of critical buckling loads ( $P_{cr}$ ) for various IPE sections and span lengths using four methods:

- Eurocode-based formulation,
- Nonlinear finite element analysis via OpenSeesPy,
- An analytical solution assuming a circular deformation path, and
- An analytical solution assuming a parabolic deformation path.

The comparisons provide insight into the accuracy, conservatism, and theoretical foundations of each approach under LTB conditions.

#### 5.1.1 Critical Buckling Load from Eurocode-3 Simplified Formula

This method, grounded in linear elastic theory, incorporates geometric properties such as the warping constant  $I_w$ , torsional constant  $I_t$ , and effective flexural stiffnesses  $I_y$  and  $I_z$ . The resulting  $M_{cr}$  is then translated to a critical vertical load  $P_{cr}$ , allowing comparison with the numerical and analytical methods.

$$M_{cr} = C_1 \frac{\pi^2 EI_y}{(kL)^2} \left\{ \sqrt{\left(\frac{k}{k_w}\right)^2 \frac{I_w}{I_y} + \frac{(kL)^2 GI_t}{\pi^2 EI_y}} + (C_2 z_g)^2 - C_2 z_g \right\} \quad (5.1)$$

When the shear center coincides with the centroid, like cross-sections with double symmetry, and when the load acts directly through the centroid, the offset  $z_g=0$ , thus eliminating the last term in the buckling formula.

Recognizing the flexural stiffness about the weak axis is defined as  $k_u = 48EI_y/L^3$ , the torsional stiffness is given by  $k_\Phi = 4GI_t/L$  and rearranging Equation 5.1.

$$M_{cr} = C_1 \frac{\pi^2 EI_y}{(kL)^2} \left\{ \sqrt{\left(\frac{k}{k_w}\right)^2 \frac{I_w}{I_y} + \frac{(kL)^2 GI_t}{\pi^2 EI_y}} \right\}$$

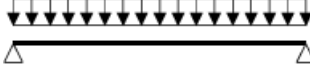
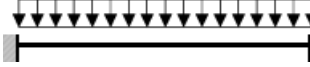
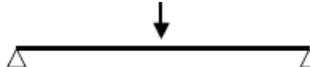
$$M_{cr} = C_1 \frac{\pi^2 EI_y}{(kL)^2} \sqrt{\frac{(kL)^2 GI_t}{\pi^2 EI_y}} \quad (5.2)$$

$$M_{cr} = C_1 \sqrt{\frac{\pi^2 EI_y}{(kL)^2} GI_t} \quad (5.3)$$

$$M_{cr} = C_1 \sqrt{\frac{\pi^2 L^2}{4 * 48} \left(\frac{48EI_y}{L^3}\right) \left(\frac{4GI_t}{L}\right)} \quad (5.4)$$

For a simply-supported beam subjected to midspan point load the shape of the bending moment diagram is triangular, and the corresponding values of the constant parameters are  $C_1 = 1.348$  and  $C_2 = 0.630$  as shown in Table 5.1. (Bureau, 2005)

Table 5.1. Values of  $C_1$  and  $C_2$  for transverse loading cases. (Bureau, 2005)

Loading and support conditions	Bending moment diagram	$C_1$	$C_2$
		1.127	0.454
		2.578	1.554
		1.348	0.630
		1.683	1.645

Note: The critical moment  $M_{cr}$  is calculated for the section with the maximum moment along the member

Therefore, substituting the values of  $C_1$ ,  $C_2$  and  $k_g$  for a simply-supported beam with doubly symmetric cross-sections subjected to a midspan point load acting directly through the centroid, the elastic critical LTB moment  $M_{cr}$  will be:

$$M_{cr} = C_1 \sqrt{\frac{\pi^2 L^2}{192} k_u k_\phi} = C_1 \cdot \frac{\pi L}{\sqrt{192}} \sqrt{k_u k_\phi} = 1.348 * \frac{\pi}{\sqrt{192}} * L \sqrt{k_u k_\phi}$$

$$M_{cr} = 0.3056 \cdot L \sqrt{k_u k_\phi} \quad (5.5)$$

To find the critical LTB point load  $P_{cr}$  at midspan of the beam corresponding to  $M_{cr}$  in Equation 5.5, the bending moment from static analysis at midspan of the simply-supported beam subjected to  $P$  (i.e.  $PL/4$ ) is equated to  $M_{cr}$ :

$$M_{cr} = \frac{P_{cr}L}{4} = 0.3056 \cdot L \sqrt{k_u k_\phi} \quad (5.6)$$

$$\begin{aligned} P_{cr} &= 4 * 0.3056 \sqrt{k_u k_\phi} \\ P_{cr} &= 1.2225 \sqrt{k_u k_\phi} \end{aligned} \quad (5.7)$$

### 5.1.2 Critical Buckling Load from Numerical Simulation (OpenSeesPy)

This method, grounded in a nonlinear geometric analysis, was conducted through a corotational beam-column formulation. The load was incrementally increased until the structure lost stability, capturing the bifurcation point corresponding to  $P_{cr}$ . This method accounts for both geometric nonlinearity and torsional-flexural interaction, offering a close-to-reality reference solution.

### 5.1.3 Critical Buckling Load from Analytical Circular Path Solution

This method approximates buckling behavior by assuming the midspan twist and lateral deflection follow a circular arc, deriving  $P_{cr}$  through energy minimization. This method generally predicted higher critical loads than the Eurocode but aligned well with OpenSees results.

Taking Equations 3.19 and 3.22 respectively:

$$k_u u - P \left( \frac{1 - \cos\phi}{\sin\phi} \right) = 0$$

$$2k_\phi\phi - Pu \left( \frac{1}{1 + \cos\phi} \right) = 0$$

To find the value of the applied load  $P$  for very small value of twist angle  $\phi$  (i.e. The critical LTB point load  $P_{cr}$ ):

- First order Taylor expansion and L' Hopital's rule are applied on the first expression above, from Equation 3.19, to avoid division by zero when calculating the limit as  $\phi$  approaches  $\phi_0 = 0$ ,

$$k_u u - P \left( \frac{1 - \cos\phi}{\sin\phi} \right) = 0$$

$$\text{Let } f(\phi) = \frac{1 - \cos\phi}{\sin\phi} \quad (5.8)$$

Using the first two terms of Taylor expansion:

$$f(\phi) = f(\phi_0) + f'(\phi_0)(\phi - \phi_0) \quad (5.9)$$

The first term of Equation 5.9:

$$f(\phi_0) = \frac{1 - \cos\phi_0}{\sin\phi_0} \quad (5.10)$$

Since division by zero can't be done the above expression can be solved by L' Hopital's rule taking the derivatives of both the numerator and denominator:

$$\lim_{\phi \rightarrow \phi_0} f(\phi) = \frac{\sin\phi_0}{\cos\phi_0} = \frac{0}{1} = 0 \quad (5.11)$$

The Second term of Equation 5.9:

$$\begin{aligned} f'(\phi) &= \frac{\sin^2\phi - \cos\phi(1 - \cos\phi)}{\sin^2\phi} \\ f'(\phi) &= \frac{\sin^2\phi + \cos^2\phi - \cos\phi}{\sin^2\phi} = \frac{1 - \cos\phi}{\sin^2\phi} = \frac{1 - \cos\phi}{1 - \cos^2\phi} \\ f'(\phi) &= \frac{1}{1 + \cos\phi} \\ f'(\phi_0) &= \frac{1}{1 + \cos\phi_0} = \frac{1}{2} \end{aligned} \quad (5.12)$$

Substituting Equations 5.11 and 5.12 into Equation 5.9:

$$f(\phi) = f(\phi_0) + f'(\phi_0)(\phi - \phi_0) = 0 + \frac{1}{2}\phi = \frac{\phi}{2} \quad (5.13)$$

Then Equation 3.19 becomes:

$$\begin{aligned} k_u u - P\left(\frac{1 - \cos\phi}{\sin\phi}\right) &= 0 \\ k_u u - P(f(\phi)) &= 0 \\ k_u u - P_{cr}\left(\frac{\phi}{2}\right) &= 0 \\ \Rightarrow P_{cr} &= \frac{2k_u u}{\phi} \end{aligned} \quad (5.14)$$

- Substituting  $\phi = \phi_0 = 0$  into Equation 3.22,

$$\begin{aligned} 2k_\phi\phi - Pu\left(\frac{1}{1 + \cos\phi}\right) &= 0 \\ 2k_\phi\phi - P_{cr}u\left(\frac{1}{1 + \cos\phi_0}\right) &= 0 \\ 2k_\phi\phi - P_{cr}u\left(\frac{1}{2}\right) &= 0 \end{aligned} \quad (5.15)$$

- Substituting the formula for  $P_{cr}$  from Equation 5.14 into the above expression:

$$\begin{aligned}
 2k_\phi\phi - \left(\frac{2k_u u}{\phi}\right)u\left(\frac{1}{2}\right) &= 0 \\
 \Rightarrow 2k_\phi\phi - \frac{k_u u^2}{\phi} &= 0 \\
 \Rightarrow 2k_\phi\phi^2 &= k_u u^2 \\
 \Rightarrow u &= \phi \sqrt{\frac{2k_\phi}{k_u}}
 \end{aligned} \tag{5.16}$$

- Solving for  $P_{cr}$  by substituting the above expression of  $u$  into Equation 5.14:

$$P_{cr} = \frac{2k_u u}{\phi} \tag{5.17}$$

$$\begin{aligned}
 \Rightarrow P_{cr} &= \frac{2k_u}{\phi} * \phi \sqrt{\frac{2k_\phi}{k_u}} \\
 \Rightarrow P_{cr} &= 2\sqrt{2} \sqrt{k_u k_\phi} = \sqrt{8k_u k_\phi}
 \end{aligned} \tag{5.18}$$

Alternatively, the critical load can be found by substituting  $\sin\phi = \phi$  and  $\cos\phi = 1$ , for very small twist  $\phi$ , into the expression of the circular deformation path shown in Equation 3.26.

$$P_{cr} = \sqrt{2k_\phi k_u \left(\phi \frac{(1+1)^2}{\phi}\right)} = \sqrt{2k_\phi k_u * 4} = \sqrt{8k_\phi k_u}$$

The expression for the critical buckling load based on the circular deformation path, shown in Equation 5.18, exhibits a strong resemblance with the Eurocode formulation, as it similarly depends on the square root of the product of the lateral bending stiffness and torsional stiffness, shown in Equation 5.7. This similarity is particularly promising, as it indicates that the underlying mechanics captured by the deformation path approach are consistent with established design standards. Such alignment not only validates the theoretical model but also suggests its potential applicability within code-based structural design frameworks.

### 5.1.4 Critical Buckling Load from Analytical Parabolic Path Solution

This method approximates buckling behavior by assuming the midspan twist and lateral deflection follow a parabolic arc, deriving  $P_{cr}$  through energy minimization. This method uses a more complex expression that incorporates an arbitrary geometric parameter  $a$  to account for the shape of the parabolic path of deflection. This formulation often produced slightly higher or lower values than the circular path solution, depending on the value of  $a$ , which in this study was constrained to a realistic positive value.

- Considering small value of  $\phi$  close to 0:

$$\text{For } \phi \rightarrow 0^+ \left\{ \begin{array}{l} \sin\phi = \phi \\ \cos\phi = 1 \\ \sin(2\phi) = 2\phi \\ \cos(4\phi) = 1 - 2\sin^2(2\phi) = 1 - 2 * (2\phi)^2 = 1 - 8\phi^2 \end{array} \right\} \quad (5.19)$$

$$\text{For } \phi \rightarrow 0^- \left\{ \begin{array}{l} \sin(-\phi) = -\phi \\ \cos(-\phi) = 1 \\ \sin(-2\phi) = -2\phi \\ \cos(-4\phi) = 1 - 2\sin^2(-2\phi) = 1 - 2 * (-2\phi)^2 = 1 - 8\phi^2 \end{array} \right\} \quad (5.20)$$

- Substituting Equations 5.19 and 5.20 into the two solutions  $P_1$  in Equation 3.47 and  $P_2$  in Equation 3.48 respectively, the critical buckling load will be:

$$\Rightarrow P_{cr} = \frac{-ah^2k_u - 8ak_\phi + hk_u + \sqrt{a^2h^4k_u^2 + 16a^2h^2k_\phi k_u + 64a^2k_\phi^2 - 2ah^3k_u^2 + 16ahk_\phi k_u + h^2k_u^2}}{4ah} \quad (5.21)$$

Here the expression for the critical buckling load based on the parabolic deformation path, in addition to the lateral bending stiffness and torsional stiffness parameters, depends on the height of the cross-section,  $h$ , and the coefficient of the parabolic path of deformation,  $a$ , as shown in Equation 5.21. Although the expression depends on only four parameters, it is much longer and complicated than the one from the circular path.

To find comparable value of the critical load with the numerical solution an appropriate value of the coefficient,  $a$ , should be chosen. The determination of this coefficient is discussed in Section 5.1.7.

### 5.1.5 Comparison of Critical Buckling Load for Various IPE Sections

To demonstrate the influence of cross-sectional properties on the lateral-torsional critical buckling capacity of beams, the critical buckling loads for various IPE sections at a fixed span length of 4.0 m were computed using the Eurocode, numerical and analytical circular path methods. The results are summarized in Table 5.2.

Table 5.2. Critical buckling loads of different IPE profiles for 4 m beam span.

Section	Critical Buckling Loads for 4 m Span (kN)			Difference (%)	
	Eurocode	Numerical	Circular Path	Numerical and Eurocode	Numerical and Circular Path
IPE 120	9.155	10.377	21.181	11.776	104.119
IPE 160	20.795	23.482	48.113	11.441	104.894
IPE 200	41.813	47.103	96.741	11.230	105.381
IPE 240	80.497	90.667	186.24	11.217	105.411
IPE 270	108.768	122.503	251.65	11.212	105.423
IPE 300	146.241	164.697	338.35	11.206	105.438

As shown in Table 5.2, all three methods show a consistent trend: the critical buckling load increases with the size of the IPE section. For example, for the IPE 120 section, the Eurocode predicts a critical load of 9.155 kN, increasing to 146.241 kN for IPE 300 section, demonstrating a nearly sixteen-fold increase in the critical buckling load due to the enhanced section properties. This is primarily related to the increased stiffness parameters, especially the second moments of area, the torsional constant, and the warping constant, as the section depth increases. These parameters directly affect both bending and torsional resistance, thus contributing to a higher resistance against LTB.

The Eurocode-based predictions are the lowest among all methods as shown in Table 5.2. For example, for the IPE 200 section, the Eurocode predicts a critical load of 41.813 kN, 47.103 kN for the numerical solution and 96.741 kN for the analytical solution based on assumed circular deformation path, reflecting the code's inherent safety factors and design conservatism.

The numerical critical load results from OpenSeesPy are consistently higher than the Eurocode values. When examining the closeness of the Eurocode and numerical solutions, a clear pattern emerges that the difference between the two shows very small decrease with

increasing section size. The deviation from the numerical solution across all section sizes is around 12%.

The analytical solution based on circular deformation path produce even higher estimates of the critical load. This indicates that while the analytical models are more physically descriptive than the Eurocode, they still reflect idealized deformation paths and omit certain parameters, like warping stiffness, present in real systems. In addition, enforcing some kinematics by forcing the structure to take a path that it does not want to take generates artificial stiffening leading to overestimates.

In contrast to the closeness of the Eurocode and numerical solutions, the critical loads from the analytical circular deformation path solution are consistently higher than the numerical critical load results from OpenSeesPy and they show a small increase in deviation as the section size increases. The deviation from the numerical solution across all section sizes is around 105%.

In summary, as the IPE section increases, all three methods show a rise in the critical buckling load, confirming that stiffness of the sections play a critical role in resisting LTB. Although the discrepancy is consistent for all sections, the theoretically insightful analytical circular path method yields very high critical buckling load predictions than the numerical method, around 105% as shown in Table 5.2, and it can be concluded that the analytical method based on circular path is not a good predictor of the critical buckling load. The numerical approach via OpenSeesPy balances realism and computational accuracy, while the Eurocode offers a practical and safe design estimate.

The critical load estimate from the parabolic deformation path is not shown here because it depends on the coefficient  $a$ , not yet determined, in addition to other geometric and stiffness parameters, as shown in Equation 5.21. The determination of the coefficient  $a$  is discussed in Section 5.2.

### 5.1.6 Comparison of Critical Buckling Load for Various Beam Spans

To demonstrate the influence of span length on the lateral-torsional critical buckling capacity of beams, the critical buckling loads for various spans for IPE 200 profile were computed using the Eurocode, numerical and analytical circular path methods. The results are summarized in Table 5.3.

Table 5.3. Critical buckling loads of IPE 200 profile beams of various spans.

Span (m)	Critical Buckling Loads for IPE 200 (kN)			Difference (%)	
	Eurocode	Numerical	Circular Path	Numerical and Eurocode	Numerical and Circular Path
2.0	167.253	188.333	386.963	11.193	105.467
3.0	74.335	83.727	171.983	11.218	105.410
4.0	41.813	47.103	96.741	11.230	105.381
5.0	26.760	30.148	61.914	11.236	105.367
6.0	18.584	20.937	42.996	11.240	105.358

All three methods show that the critical buckling load decreases as the span length of the beam increases as shown in Table 5.3. For example, for span of 2.0 m, the analytical circular path solution predicts a critical load of 386.963 kN which decreases to 42.996 kN for a span length of 6.0 m. This is primarily related to increased lateral instability because of longer laterally unsupported span reducing the stiffnesses of the beam for LTB.

The Eurocode-based predictions are the lowest among all methods. When examining the closeness of the Eurocode and numerical solutions, a clear pattern emerges that the difference between the two follows a nearly parallel trend remaining about 11% as shown in Table 5.3.

In contrast, the critical loads from analytical solutions based on circular deformation path are consistently higher than the numerical values following a nearly parallel trend. When examining their closeness, a clear pattern emerges that the difference between the two is about 105%, which is very large, as shown in Table 5.3.

In summary, as the span length increases, all three methods show a drop in the critical buckling load, confirming that span length of the beam affect the stiffness hence the LTB resistance. Once again it is shown that the analytical method based on circular deformation path is not a good predictor of the critical buckling load as the difference with the numerical method in critical load estimation is very large which is about 105% as shown in Table 5.3.

## 5.2 DETERMINATION OF THE COEFFICIENT OF PARABOLIC PATH SOLUTION

As described in Sections 5.1.5 and 5.1.6, the analytical solution based on circular deformation path is not a good predictor of the critical buckling load, therefore it is necessary to find the coefficient,  $a$ , for the alternative analytical solution based on parabolic deformation path by using the critical buckling load expression for parabolic path shown in Equation 5.21 to match the critical buckling loads from the numerical solution shown in Table 5.2 and Table 5.3.

To demonstrate the influence of cross-sectional properties on the value of the coefficient,  $a$ , of the parabolic path, the values of the coefficient for various IPE sections at a fixed span length of 4.0 m are computed by trial and error. The results are summarized in Table 5.4.

**Table 5.4.** Coefficient,  $a$ , of different IPE sections for 4.0 m beam span.

Section	$h$ (mm)	$k_u$ (N/mm)	$k_\phi$ (Nmm)	$a$ (1/mm)
IPE 120	120	41.505	1351200	0.00187
IPE 160	160	102.465	2824000	0.00186
IPE 200	200	213.60	5476800	0.00169
IPE 240	240	425.40	10192000	0.00143
IPE 270	270	629.85	12568000	0.00110
IPE 300	300	905.70	15800000	0.000695

The value of the coefficient,  $a$ , for various spans of IPE 200 profile are computed by trial and error to demonstrate the influence of the span length on the value of the coefficient. The results are summarized in Table 5.5.

**Table 5.5.** Coefficient,  $a$ , for IPE 200 profile beams of various spans.

$L$ (mm)	$h$ (mm)	$k_u$ (N/mm)	$k_\phi$ (Nmm)	$a$ (1/mm)
2000	200	1708.8	10953600	0.00069
3000	200	506.311	7302400	0.00167
4000	200	213.60	5476800	0.00169
5000	200	109.363	4381440	0.001524
6000	200	63.289	3651200	0.00135

Calculating the critical load for the parabolic path using Equation 5.21 with the coefficients,  $a$ , from Table 5.4 and Table 5.5 gives the same critical buckling loads as the ones from the numerical solution shown in Table 5.2 and 5.3 respectively.

### 5.3 COMPARISON OF POST-BUCKLING RESPONSE

The two analytical methods based on two distinct assumed deformation paths predict an approximate LTB response of the simply-supported IPE-beam under the given loading and boundary conditions.

The OpenSeesPy simulation provide detailed, nonlinear results for LTB of steel IPE sections under various lengths and section sizes. The simulations capture the critical buckling load as well as the associated lateral deflection, torsional twist, and vertical deflection under applied loads.

#### 5.3.1 Comparison of Post-Buckling Response for Various IPE Sections

To demonstrate the influence of cross-sectional properties on the post-buckling response of beams, the deflection and torsional responses for gradually increasing load considering various IPE sections at a fixed span length of 4.0 meters are computed using the analytical methods based on assumed deformation paths and the numerical method. The results are shown in plots of load vs deflection, load vs twist and deformed shapes.

For the analytical solution based on the parabolic path assumption, the coefficient,  $a$ , is calculated applying the critical buckling load expression shown in Equation 5.21 to match the critical buckling load from the numerical method. The values of  $a$  used in the plots below are shown in Table 5.4.

**(a) Applied Load vs. Lateral Deflection.** The equilibrium paths showing the lateral deflection for gradually increasing midspan point load for six IPE profiles, with smaller section of IPE 120 upto IPE 300 section, for a simply-supported beam of length 4.0 meters are shown in Figures 5.1 to 5.6.

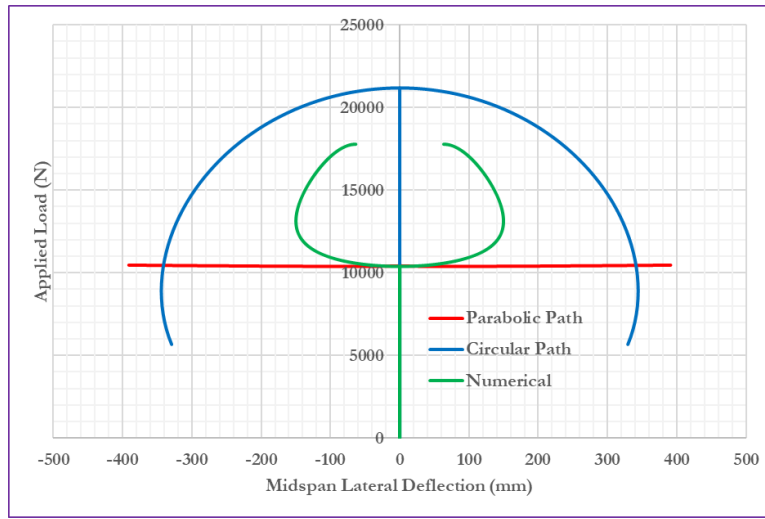


Figure 5.1. Applied Load vs. Lateral Deflection for IPE 120 Profile with Span of 4.0 m.

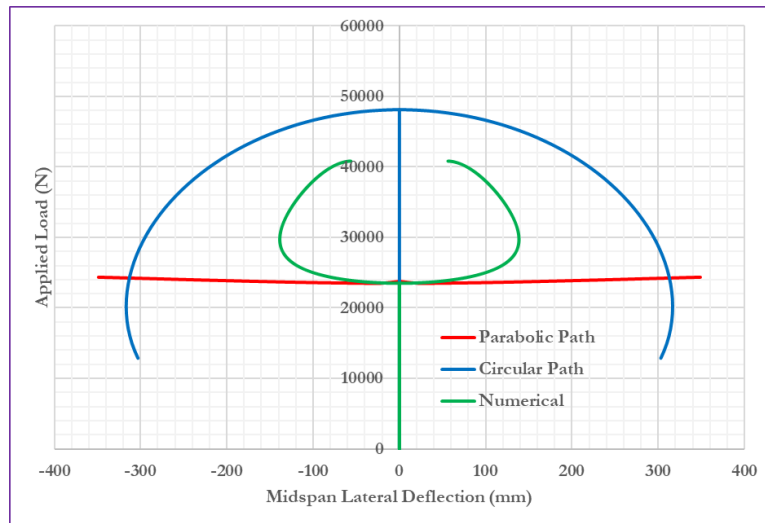


Figure 5.2. Applied Load vs. Lateral Deflection for IPE 160 Profile with Span of 4.0 m.

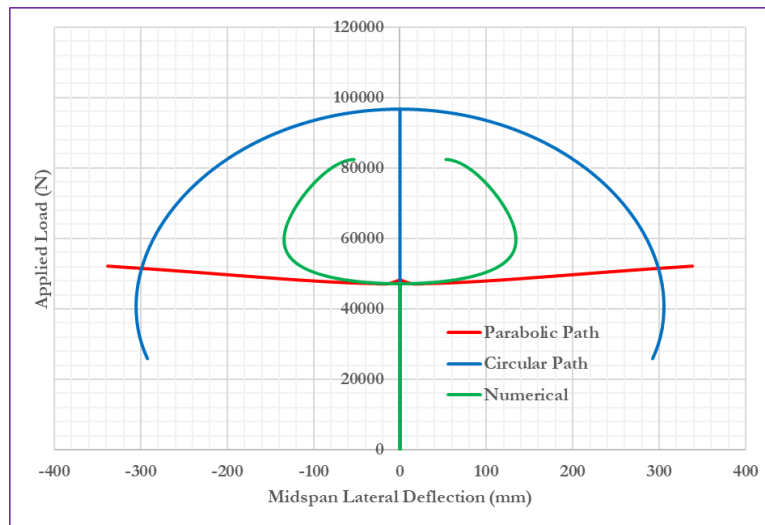


Figure 5.3. Applied Load vs. Lateral Deflection for IPE 200 Profile with Span of 4.0 m.

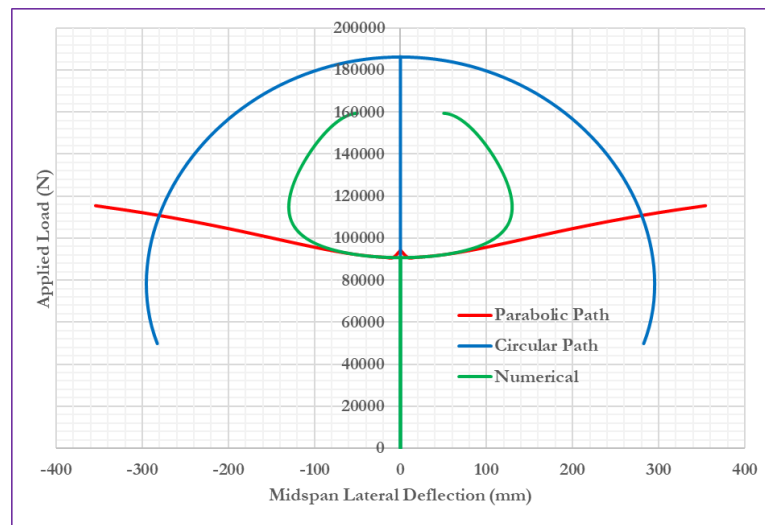


Figure 5.4. Applied Load vs. Lateral Deflection for IPE 240 Profile with Span of 4.0 m.

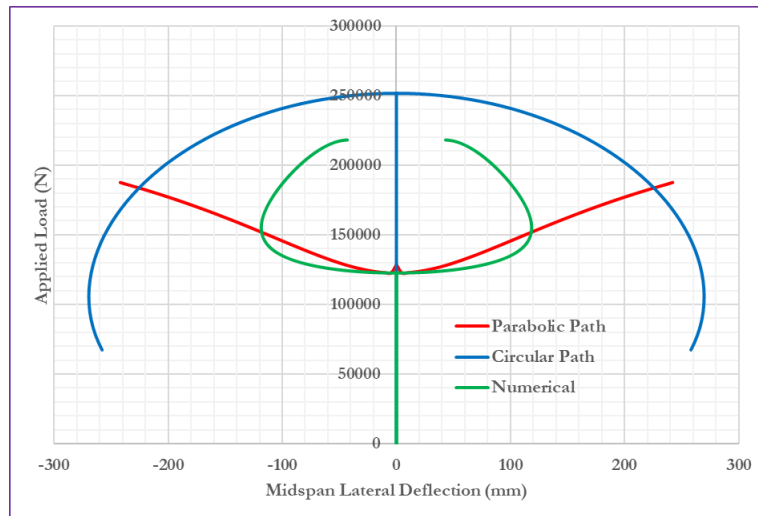


Figure 5.5. Applied Load vs. Lateral Deflection for IPE 270 Profile with Span of 4.0 m.

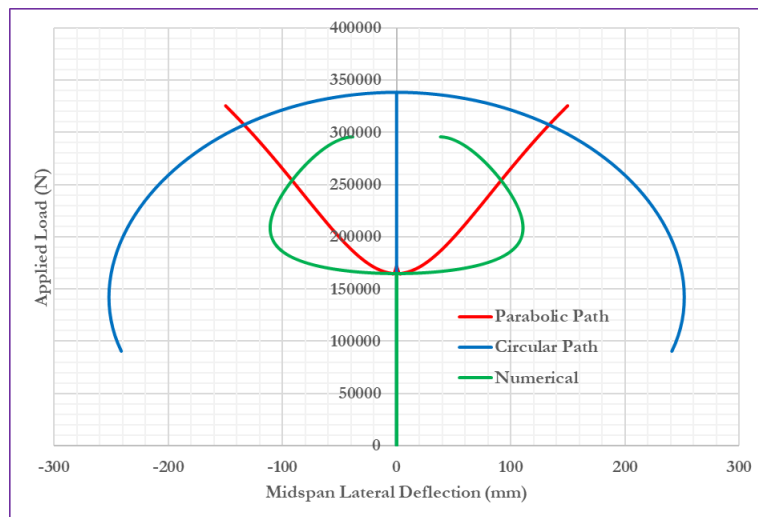


Figure 5.6. Applied Load vs. Lateral Deflection for IPE 300 Profile with Span of 4.0 m.

The applied load vs. lateral deflection plots from the analytical solution based on circular deformation paths, shown by the blue lines in Figures 5.1 to 5.6, exhibit a subcritical response in the post-buckling region, showing softening where there is an increase in

displacement with decreasing applied load. Both the critical load and the post-buckling response are very different from the numerical solution for all section sizes.

In contrast, the ones from the analytical solution based on parabolic deformation path and the numerical simulation, shown by the red and green lines respectively in Figures 5.1 to 5.6, display supercritical post-buckling response, showing hardening where there is an increase in displacement with increasing applied load, for all sections. The slope of the post-buckling response increases with section size. For example, for IPE 120 and IPE 160 sections the post-buckling response is nearly horizontal as shown in Figures 5.1 and 5.2, whereas for IPE 270 and IPE 300 sections the slope becomes steep as shown in Figures 5.5 and 5.6.

For smaller sections, although the post-buckling response from the parabolic deformation path has gentle slope, initially it is analogous to the numerical solution with similar critical load. Initially the post-buckling response from the parabolic deformation path solution gets closer to the numerical solution as the section size increases from IPE 120 to IPE 240 profile as shown in Figures 5.1 to 5.4. But further increase in the section size increases the difference between the numerical and parabolic path solutions as shown in Figures 5.5 and 5.6 for IPE 270 and IPE 300 sections, even though they have similar critical load.

**(b) Applied Load vs. Torsional Twist.** The equilibrium paths showing the torsional twist for gradually increasing midspan point load for six IPE profiles, with smaller section of IPE 120 upto IPE 300 section, for a simply-supported beam of length 4.0 meters are shown in Figures 5.7 to 5.12.

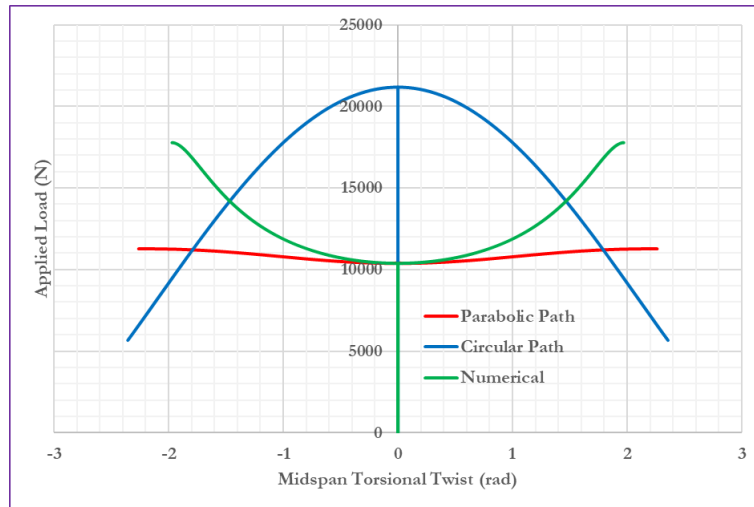


Figure 5.7. Applied Load vs. Torsional Twist for IPE 120 Profile with Span of 4.0 m.

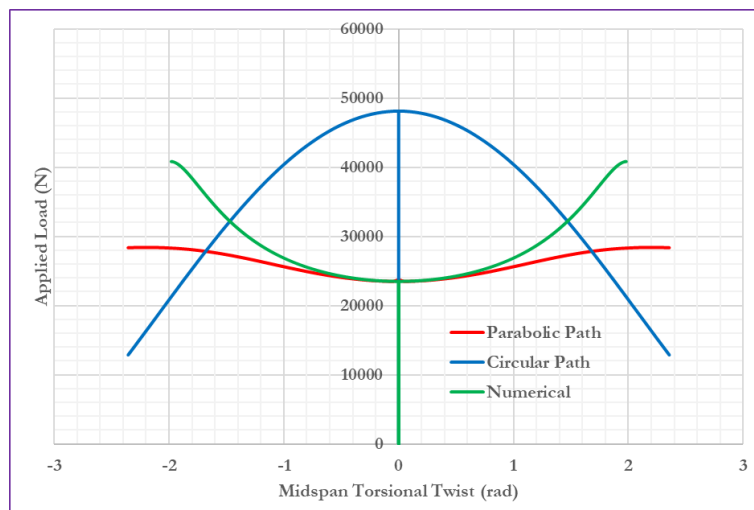


Figure 5.8. Applied Load vs. Torsional Twist for IPE 160 Profile with Span of 4.0 m.

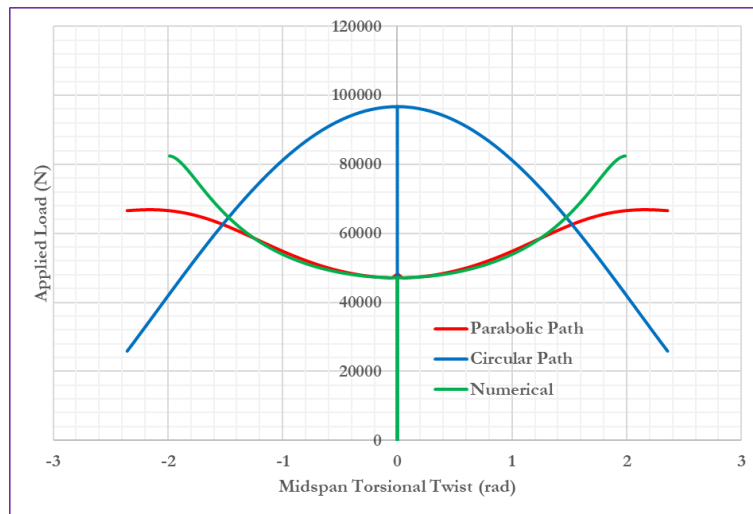


Figure 5.9. Applied Load vs. Torsional Twist for IPE 200 Profile with Span of 4.0 m.

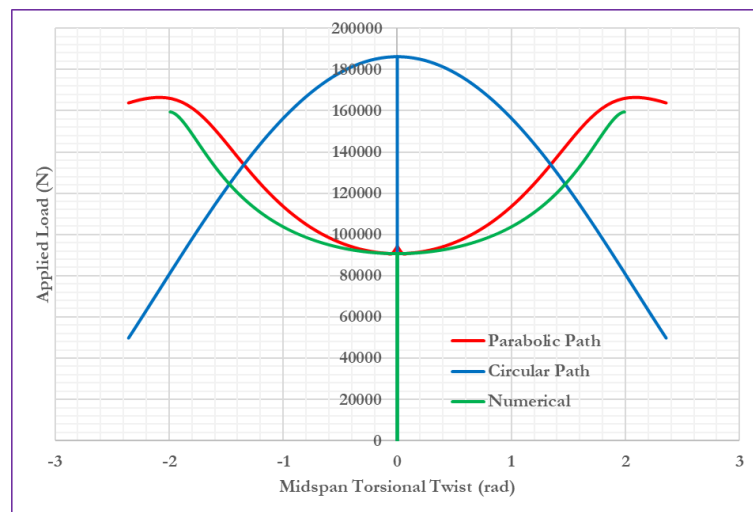


Figure 5.10. Applied Load vs. Torsional Twist for IPE 240 Profile with Span of 4.0 m.

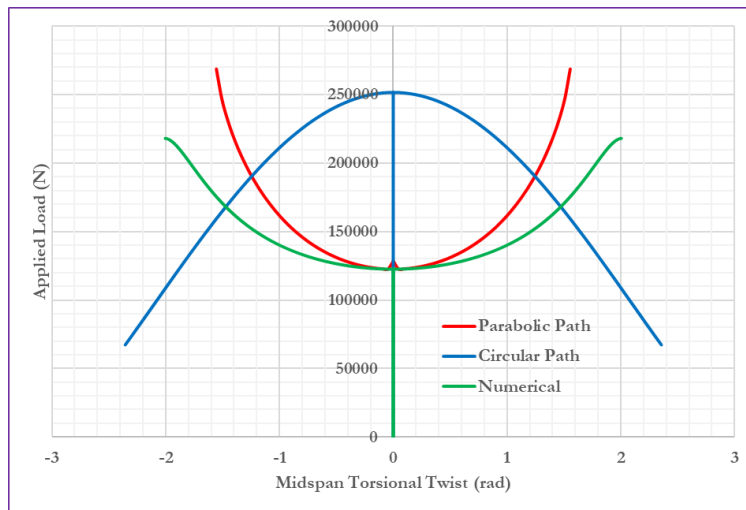


Figure 5.11. Applied Load vs. Torsional Twist for IPE 270 Profile with Span of 4.0 m.

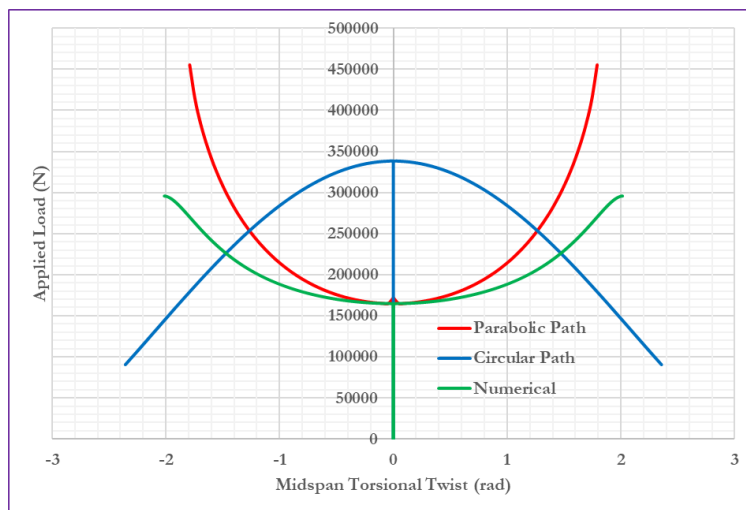


Figure 5.12. Applied Load vs. Torsional Twist for IPE 300 Profile with Span of 4.0 m.

Like the discussion in (a) for the applied load vs. lateral deflection plots, the applied load vs. torsional twist plots from the analytical solution based on circular deformation paths, shown by the blue lines in Figures 5.7 to 5.12, exhibit a subcritical response in the post-buckling region. Both the critical load and the post-buckling response are very different from the numerical solution for all section sizes because the formulation based on circular

deformation path assumption is not a good predictor of critical buckling load than the parabolic one.

In contrast, the plots from the analytical solution based on parabolic deformation path and the numerical simulation, shown by the red and green lines respectively in Figures 5.7 to 5.12, display supercritical post-buckling response.

From the figures it is visible that the post-buckling response from the parabolic deformation path solution gets closer to the numerical solution as the section size increases from IPE 120 to IPE 200 as shown in Figures 5.7 to 5.9. For IPE 200 section the numerical and the parabolic path solutions have better matching as shown in Figure 5.9. Finally for IPE 240 to IPE 300 profiles, the post-buckling behavior ends up above the numerical solution with an increasing gap for larger twist, though they have similar critical buckling load and initial post-buckling response, as shown in Figures 5.10 to 5.12.

**(c) Applied Load vs. Vertical Deflection.** The equilibrium paths showing the vertical deflection for gradually increasing midspan point load for six IPE profiles, with smaller section of IPE 120 upto IPE 300 section, for a simply-supported beam of length 4.0 meters are shown in Figures 5.13 to 5.18.

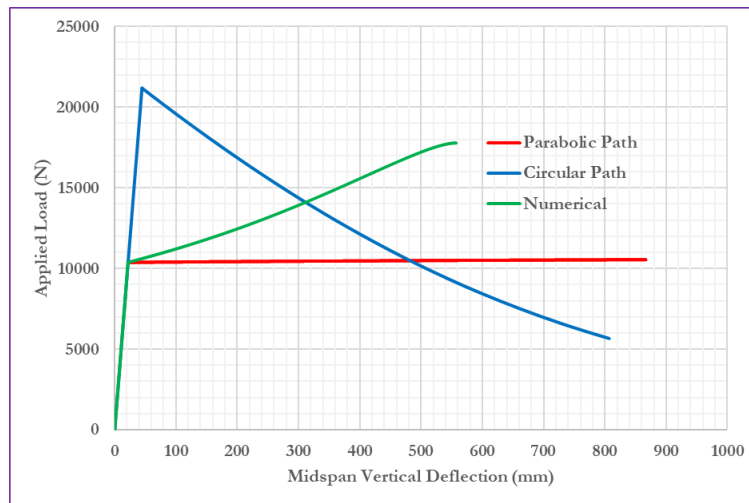


Figure 5.13. Applied Load vs. Vertical Deflection for IPE 120 Profile with Span of 4.0 m.

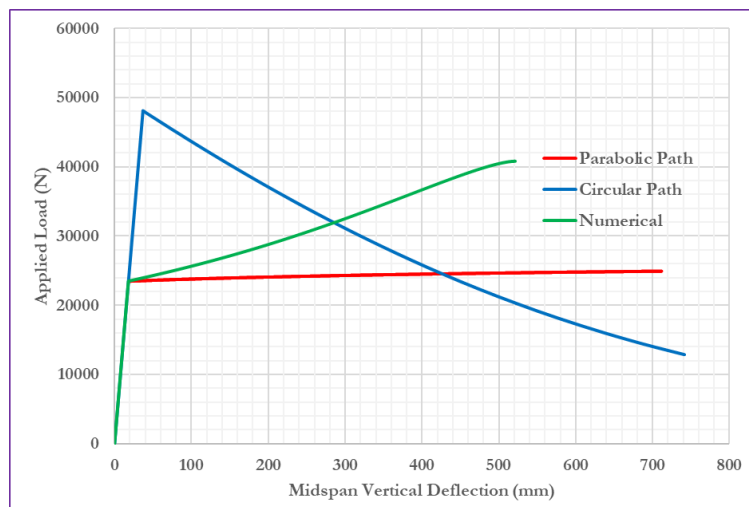


Figure 5.14. Applied Load vs. Vertical Deflection for IPE 160 Profile with Span of 4.0 m.

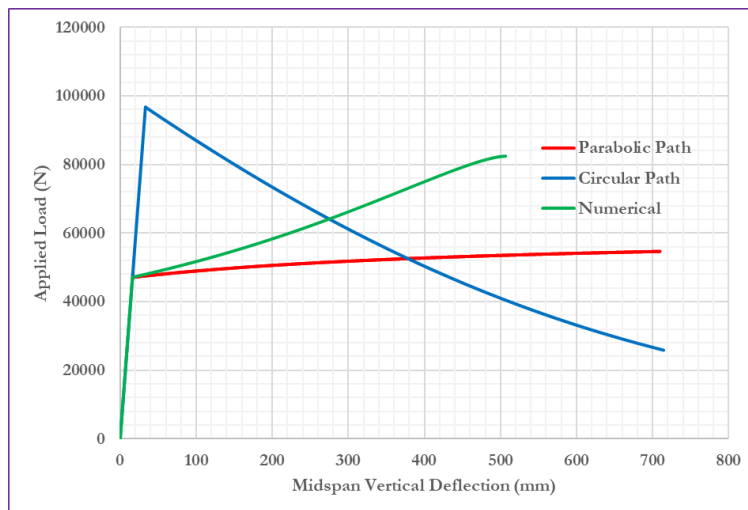


Figure 5.15. Applied Load vs. Vertical Deflection for IPE 200 Profile with Span of 4.0 m.

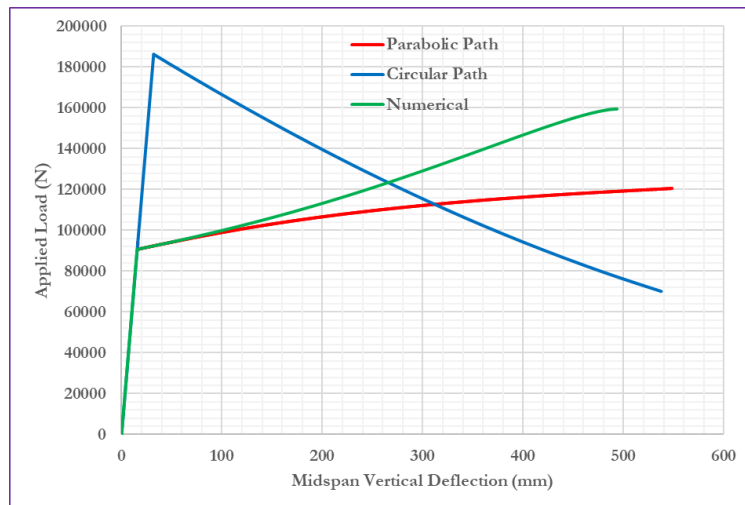


Figure 5.16. Applied Load vs. Vertical Deflection for IPE 240 Profile with Span of 4.0 m.

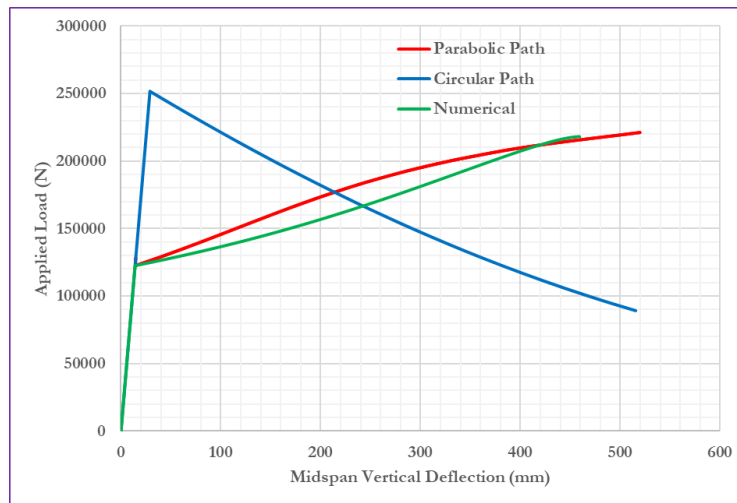


Figure 5.17. Applied Load vs. Vertical Deflection for IPE 270 Profile with Span of 4.0 m.

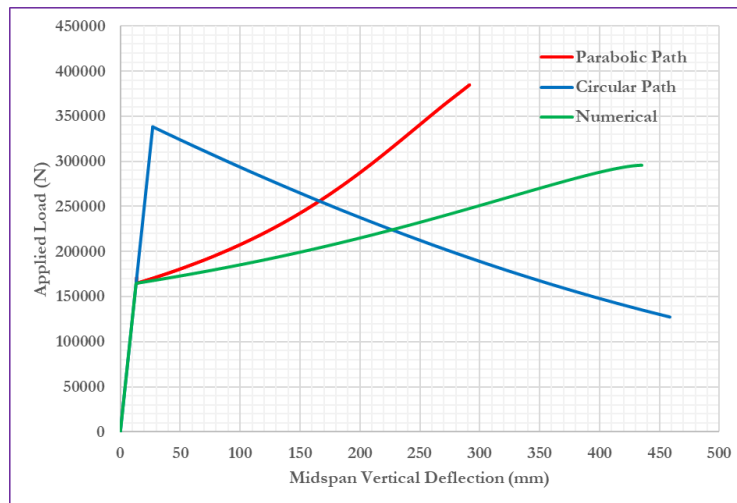


Figure 5.18. Applied Load vs. Vertical Deflection for IPE 300 Profile with Span of 4.0 m.

As shown by the blue lines in Figures 5.13 to 5.18, the applied load vs. vertical deflection plots from the analytical solution based on circular deformation path shows softening in the post-buckling region, with very different critical load and post-buckling response from the numerical solution, for all section sizes, while the ones from the analytical solution

based on parabolic deformation path and the numerical simulation, shown by the red and green lines respectively, display hardening.

The slope of the post-buckling response increases with section size for the parabolic path solution. For example, for IPE 120 and IPE 160 sections the post-buckling response is nearly horizontal as shown in Figures 5.13 and 5.14, whereas for IPE 270 and IPE 300 sections the slope becomes steeper as shown in Figures 5.17 and 5.18.

The post-buckling response from the parabolic deformation path solution gets closer to the numerical solution as the section size increases from IPE 120 to IPE 270 profile as shown in Figures 5.13 to 5.17. But further increase in the section size increases the difference between the numerical and parabolic path solutions as shown in Figures 5.18 for IPE 300 section, even though the critical load is the same.

Moreover, note that the load-deflection curves in the post-buckling region of the analytical solution based on parabolic deformation path is below the numerical solution for smaller to medium section sizes, as shown in Figures 5.13 to 5.16 for IPE 120 to IPE 240 profiles, and is above the numerical solution for larger profiles, as shown in Figures 5.17 and 5.18 for IPE 270 and IPE 300 sections.

**(d) Deformed Shapes (Vertical vs. Lateral Deflection).** The deformed shapes showing the plots of the midspan vertical deflections vs. midspan lateral deflections for six IPE profiles, with smaller section of IPE 120 upto IPE 300 section, for a simply-supported beam of length 4.0 meters are shown in Figures 5.19 to 5.24.

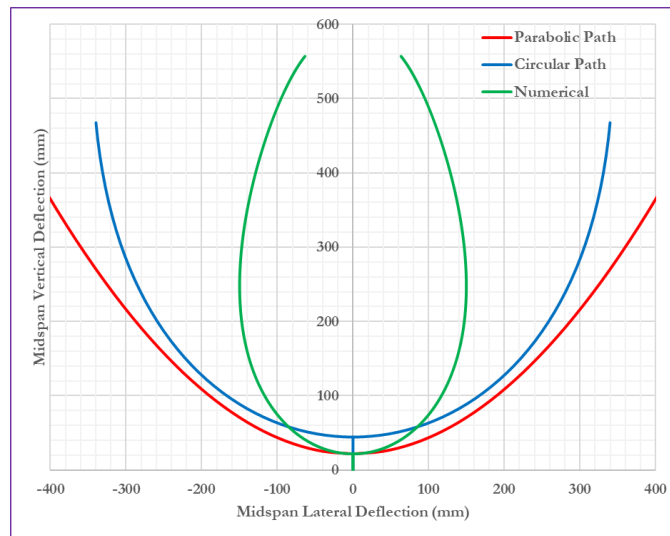


Figure 5.19. Vertical vs. Lateral Deflection for IPE 120 Profile with Span of 4.0 m.

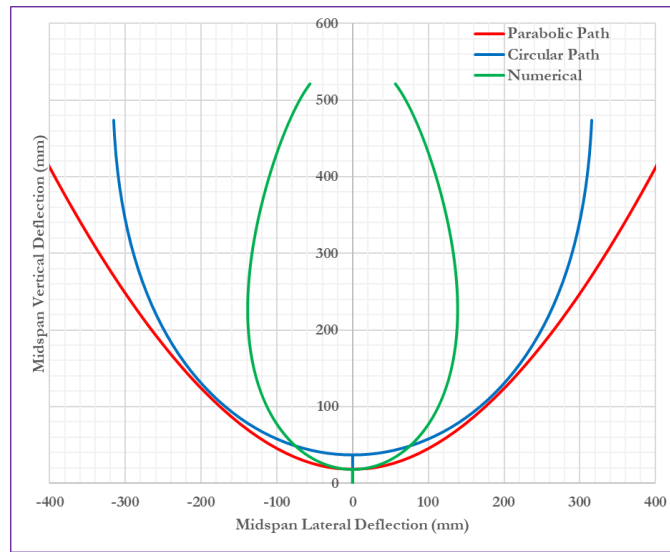


Figure 5.20. Vertical vs. Lateral Deflection for IPE 160 Profile with Span of 4.0 m.

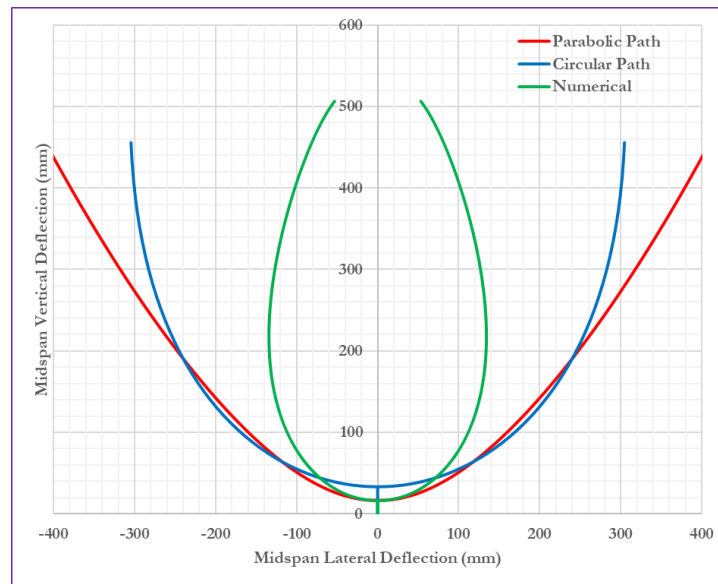


Figure 5.21. Vertical vs. Lateral Deflection for IPE 200 Profile with Span of 4.0 m.

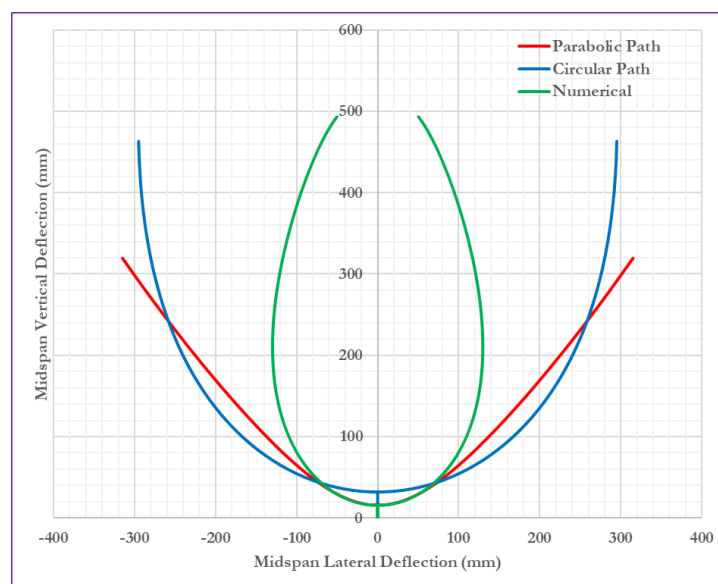


Figure 5.22. Vertical vs. Lateral Deflection for IPE 240 Profile with Span of 4.0 m.

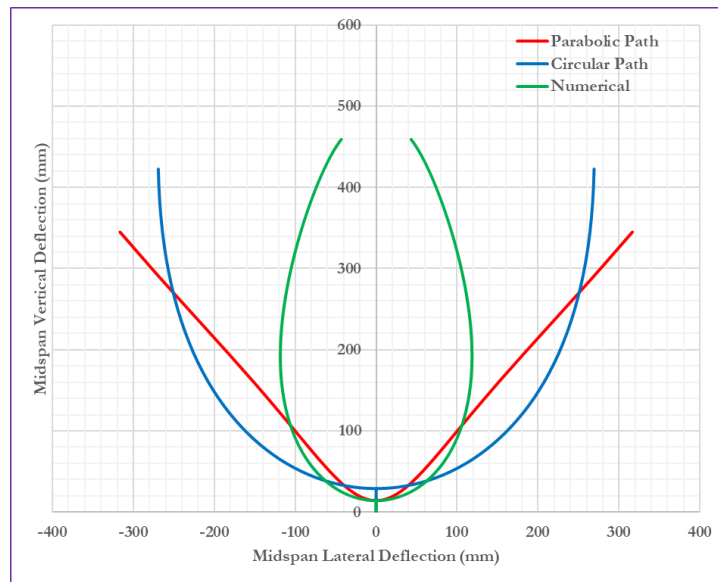


Figure 5.23. Vertical vs. Lateral Deflection for IPE 270 Profile with Span of 4.0 m.

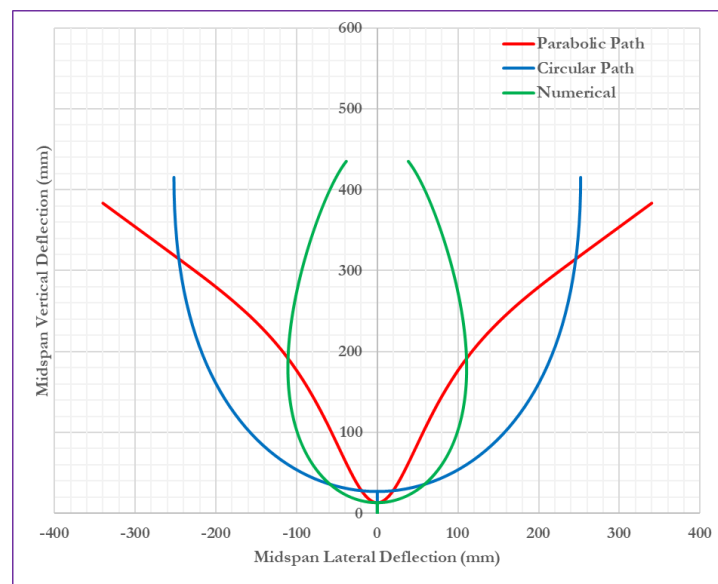


Figure 5.24. Vertical vs. Lateral Deflection for IPE 300 Profile with Span of 4.0 m.

The deformed shapes, showing plot of vertical deflection vs lateral deflection, for the analytical method based on the circular deformation path completely disagree with the numerical solutions for all section sizes, even though they are qualitatively similar, as shown in Figures 5.19 to Figure 5.24.

The agreement between the deformed shapes from the analytical method based on the parabolic deformation path with the numerical one is different across different sections. As the section size increases from IPE 120 to IPE 240 profile the deformed shapes from the parabolic path get closer to the numerical deformed shapes as shown in Figures 5.19 to 5.22. For IPE 240 section the numerical and the parabolic path deformed shapes have better initial matching in the post-buckling region as shown in Figure 5.22. This matching in the deformed shapes doesn't exist for IPE 270 and IPE 300 profiles as shown in Figures 5.23 and 5.24.

### 5.3.2 Comparison of Post-Buckling Response for Various Beam Spans

To demonstrate the influence of span length on the post-buckling response of beams, the deflection and torsional responses for gradually increasing load considering various spans for IPE 200 profile are computed using the analytical methods based on assumed deformation paths and the numerical method. The results are shown in plots of load vs deflection, load vs twist and deformed shapes.

For the analytical solution based on the parabolic path assumption, the coefficient,  $a$ , is calculated using Equation 5.22 derived in the previous section and the values of  $a$  used in the plots below are shown in Table 5.5.

**(a) Applied Load vs. Lateral Deflection.** The equilibrium paths showing the lateral deflection for gradually increasing midspan point load for a simply-supported steel IPE 200 profile beam of span length from 2.0 m to 6.0 m are shown in Figures 5.25 to 5.29.

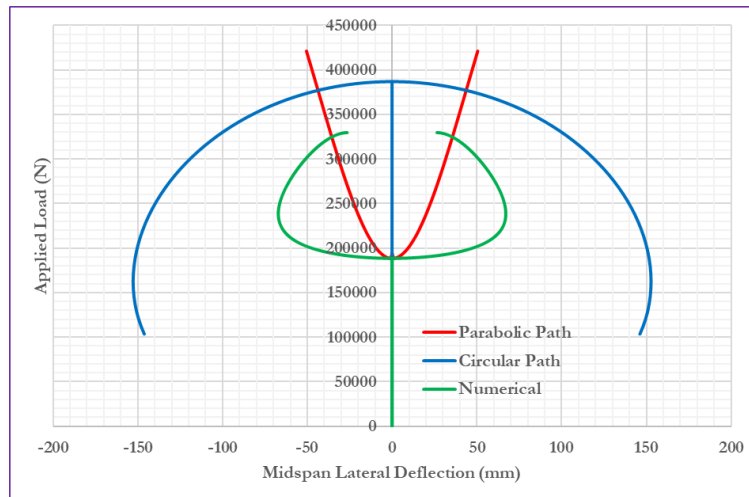


Figure 5.25. Applied Load vs. Lateral Deflection for IPE 200 Profile with Span of 2.0 m.

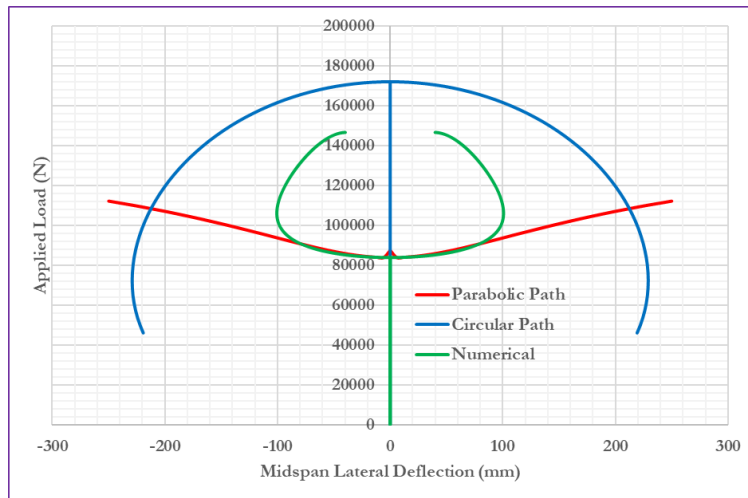


Figure 5.26. Applied Load vs. Lateral Deflection for IPE 200 Profile with Span of 3.0 m.

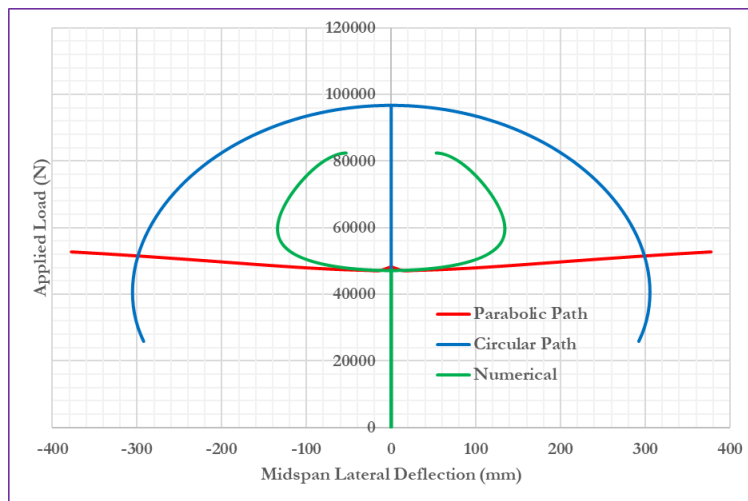


Figure 5.27. Applied Load vs. Lateral Deflection for IPE 200 Profile with Span of 4.0 m.

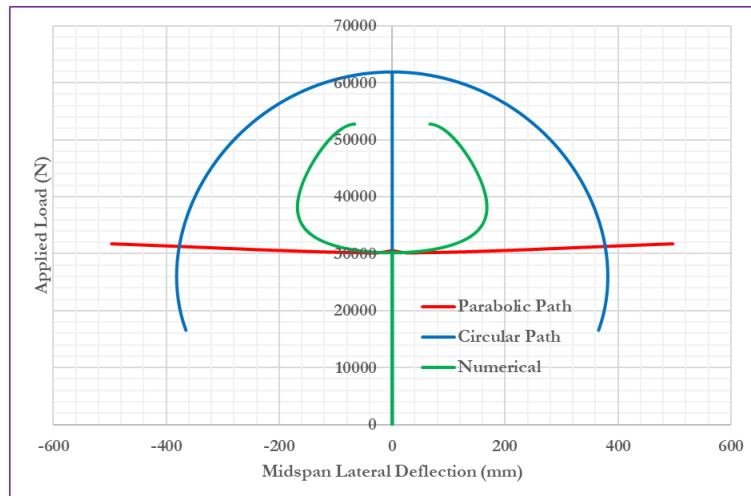


Figure 5.28. Applied Load vs. Lateral Deflection for IPE 200 Profile with Span of 5.0 m.

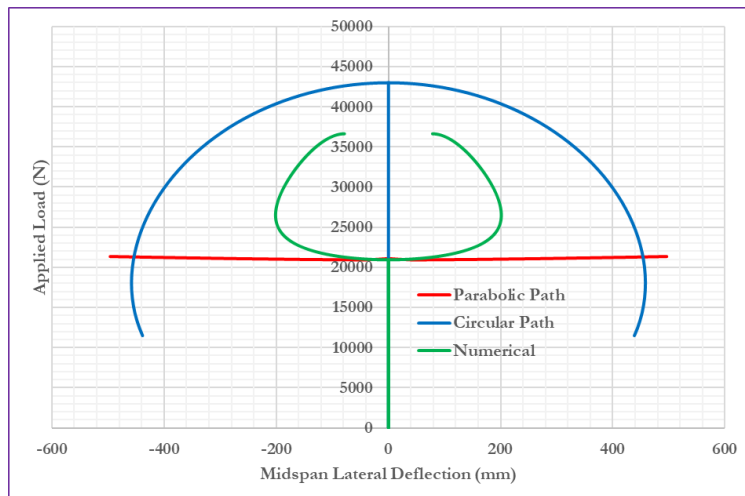


Figure 5.29. Applied Load vs. Lateral Deflection for IPE 200 Profile with Span of 6.0 m.

The applied load vs. lateral deflection plots from the analytical solution based on circular deformation paths, shown by the blue lines in Figures 5.25 to 5.29, exhibit a subcritical response in the post-buckling region. Both the critical load and the post-buckling response are very different from the numerical solution for all beam spans.

In contrast, the ones from the analytical solution based on parabolic deformation path and the numerical simulation, shown by the red and green lines respectively in Figures 5.25 to 5.29, display supercritical post-buckling response for all sections. The slope of the post-buckling response decreases with increasing span length. For example, for beam span of 2.0 m the post-buckling response has steep slope as shown in Figures 5.25, whereas for beam spans of 5.0 m and 6.0 m the slope becomes gentle and nearly horizontal as shown in Figures 5.28 and 5.29.

For larger spans, although the post-buckling response from the parabolic deformation path has gentle slope, initially it is analogous to the numerical solution with similar critical load as shown in Figures 5.27, 5.28 and 5.29 for beam spans of 4.0 m, 5.0 m and 6.0 m respectively. But for smaller beam spans the gap between the numerical and parabolic path increases for large lateral deflection as shown in Figures 5.25 for beam span of 2.0 m, even though they have similar critical load. For IPE 200 beam with a span of 3.0 m the numerical and the parabolic path lateral deflection responses have better initial matching in the post-buckling region as shown in Figure 5.26.

**(b) Applied Load vs. Torsional Twist.** The equilibrium paths showing the torsional twist for gradually increasing midspan point load for a simply-supported steel IPE 200 profile beam of span length from 2.0 m to 6.0 m are shown in Figures 5.30 to 5.34.

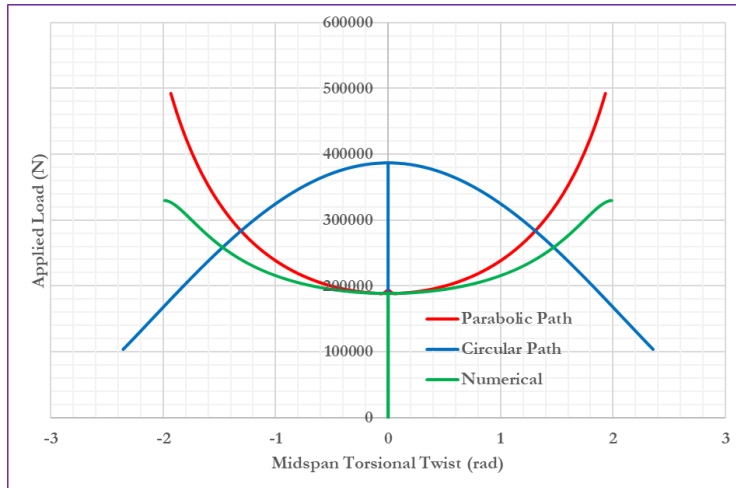


Figure 5.30. Applied Load vs. Torsional Twist for IPE 200 Profile with Span of 2.0 m.

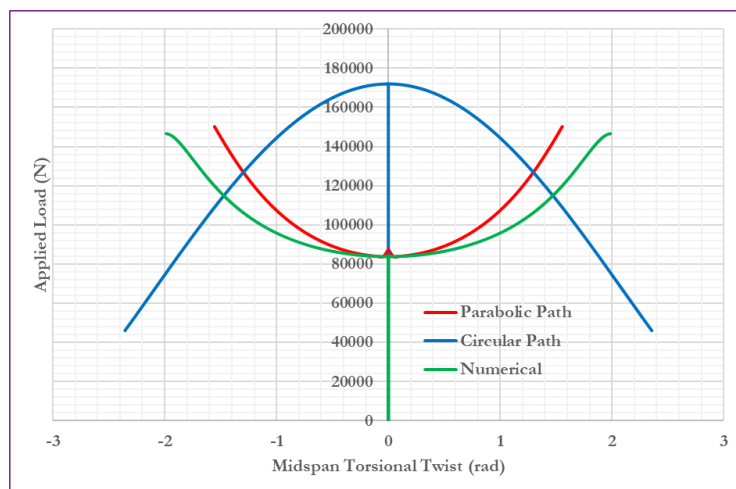


Figure 5.31. Applied Load vs. Torsional Twist for IPE 200 Profile with Span of 3.0 m.

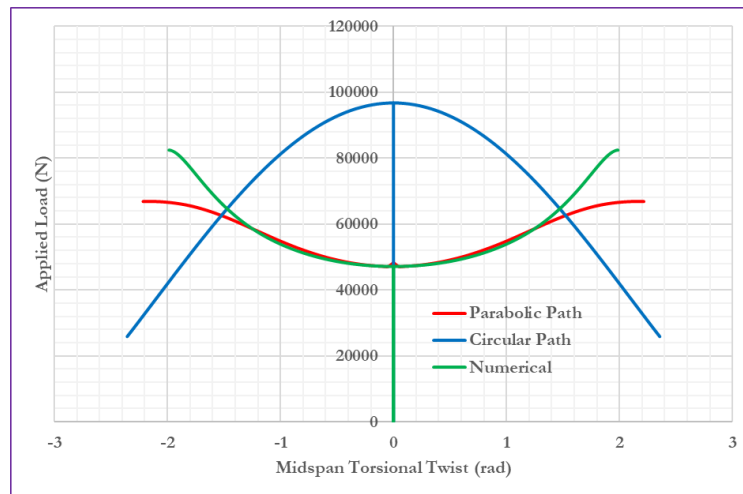


Figure 5.32. Applied Load vs. Torsional Twist for IPE 200 Profile with Span of 4.0 m.

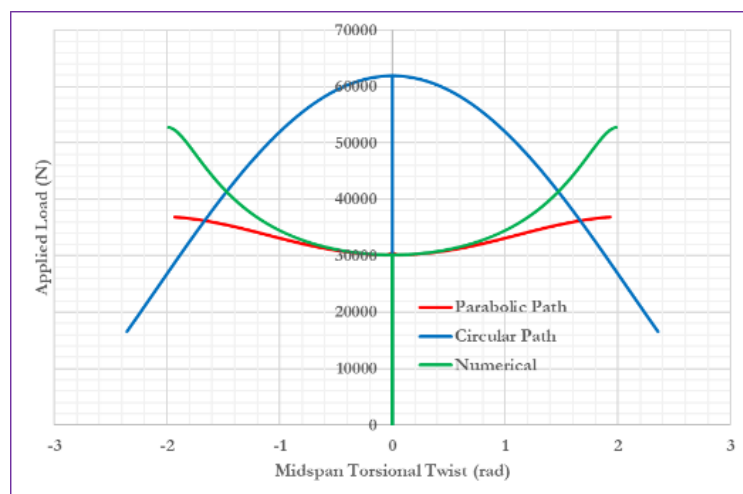


Figure 5.33. Applied Load vs. Torsional Twist for IPE 200 Profile with Span of 5.0 m.

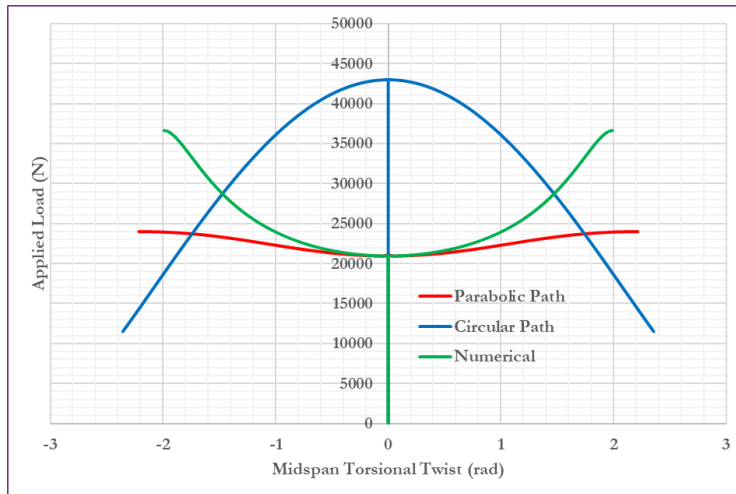


Figure 5.34. Applied Load vs. Torsional Twist for IPE 200 Profile with Span of 6.0 m.

Like the discussion in (a) for the applied load vs. lateral deflection plots, the applied load vs. torsional twist plots from the analytical solution based on circular deformation paths, shown by the blue lines in Figures 5.30 to 5.34, exhibit a subcritical response in the post-buckling region. Both the critical load and the post-buckling response are very different from the numerical solution for all beam spans

In contrast, the plots from the analytical solution based on parabolic deformation path and the numerical simulation, shown by the red and green lines respectively in Figures 5.30 to 5.34, display supercritical post-buckling response.

From Figures 5.30 and 5.31 it is visible that the post-buckling response from the parabolic deformation path solution starts above and ends up below the numerical solution by slowly changing its slope from steep to gentler one as the beam span increases from 3.0 m to 6.0 m.

The initial part of the post-buckling region is analogous to the numerical solution for all beam spans. Note in Figure 5.32 that the post-buckling response of the 4.0 m span beam from the parabolic path solution shows a very good agreement with the numerical solution. Finally for 5.0 m and 6.0 beam spans, the post-buckling behavior ends up below the numerical solution with an increasing gap for larger twist, nevertheless they have similar critical buckling load and initial post-buckling response, as shown in Figures 5.33 and 5.34.

**(c) Applied Load vs. Vertical Deflection.** The equilibrium paths showing the vertical deflection for gradually increasing midspan point load for a simply-supported steel IPE 200 profile beam of span length from 2.0 m to 6.0 m are shown in Figures 5.35 to 5.39.

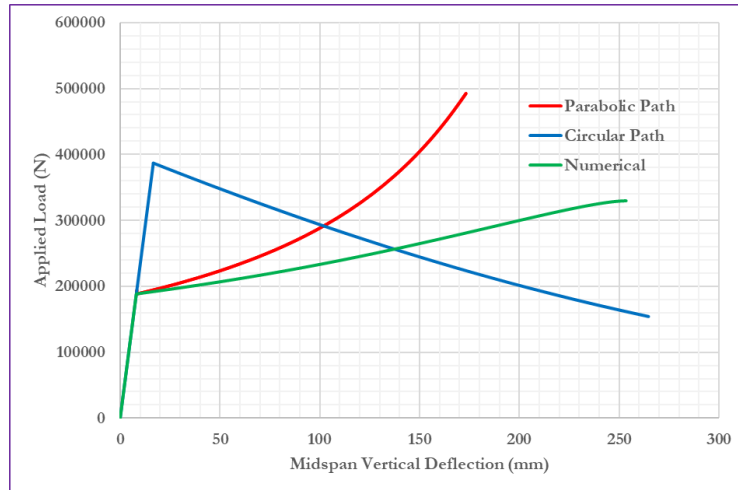


Figure 5.35. Applied Load vs. Vertical Deflection for IPE 200 Profile with Span of 2.0 m.

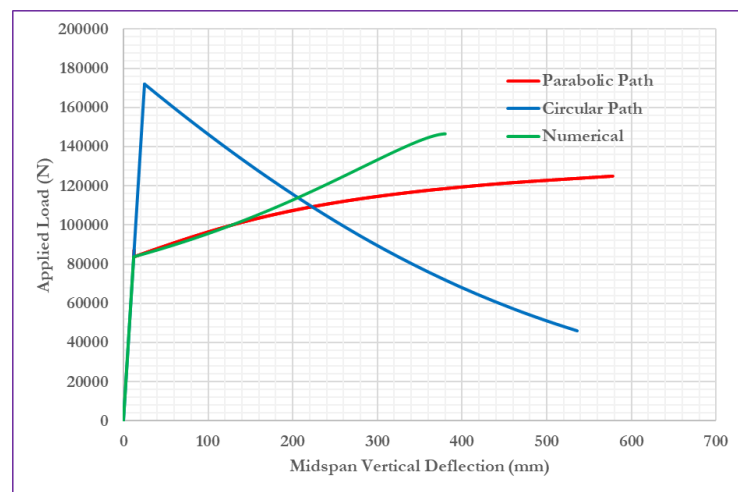


Figure 5.36. Applied Load vs. Vertical Deflection for IPE 200 Profile with Span of 3.0 m.

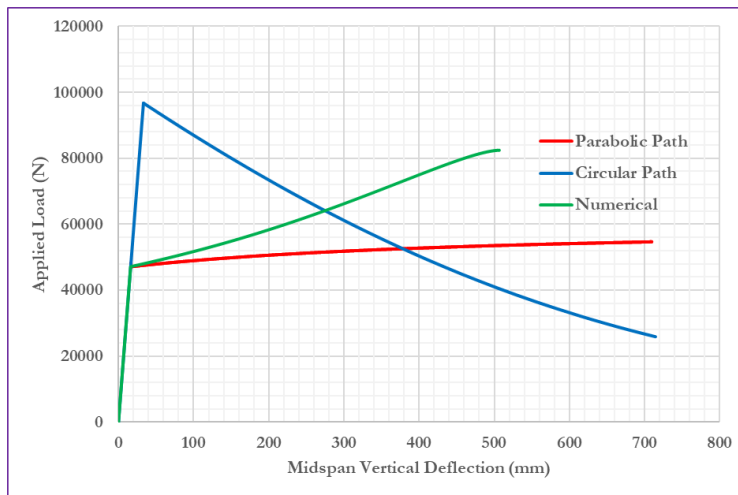


Figure 5.37. Applied Load vs. Vertical Deflection for IPE 200 Profile with Span of 4.0 m.

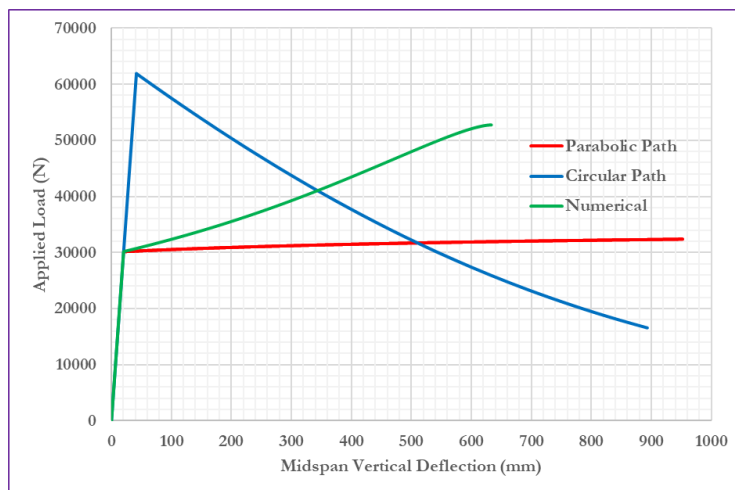
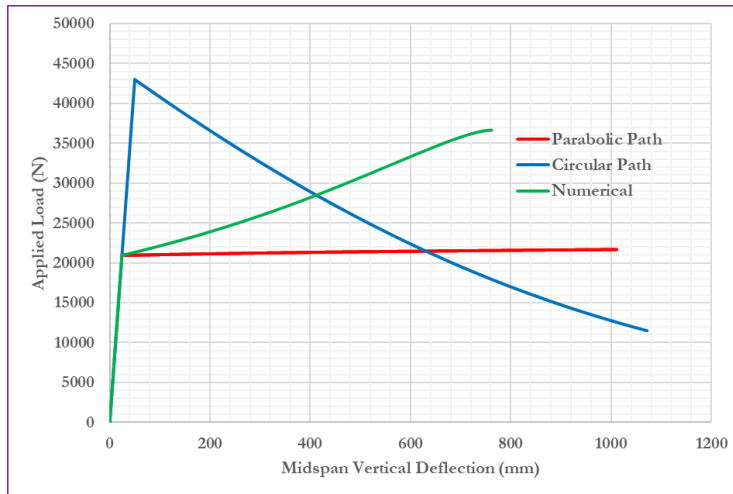


Figure 5.38. Applied Load vs. Vertical Deflection for IPE 200 Profile with Span of 5.0 m.



**Figure 5.39. Applied Load vs. Vertical Deflection for IPE 200 Profile with Span of 6.0 m.**

As shown by the blue lines in Figures 5.35 to 5.39, the applied load vs. vertical deflection plots from the analytical solution based on circular deformation path shows softening in the post-buckling region, with very different critical load and post-buckling response from the numerical solution, for all section sizes, while the ones from the analytical solution based on parabolic deformation path and the numerical simulation, shown by the red and green lines respectively, display hardening.

The slope of the post-buckling response decreases with increasing beam span for the parabolic path solution. For example, for 2.0 m beam span the post-buckling response has steep slope as shown in Figures 5.35, whereas for 5.0 m and 6.0 m beam spans the slope becomes nearly horizontal as shown in Figures 5.38 and 5.39 respectively.

The initial part of the post-buckling response from the parabolic deformation path solution gets closer to the numerical solution as the beam span increases from 2.0 m to 3.0 m as shown in Figures 5.35 and 5.36. But further increase in the span length increases the difference between the numerical and parabolic path solutions as shown in Figures 5.38 and 5.39 for 5.0 m and 6.0 m beam spans, even though they have similar critical load.

Moreover, note that the load-deflection curves in the post-buckling region of the analytical solution based on parabolic deformation path is above the numerical solution for shorter beam span, as shown in Figures 5.35 for 2.0 m beam span, and is below the numerical solution for longer beam spans, as shown in Figures 5.38 and 5.39 for 5.0 m and 6.0 m beam spans respectively.

**(d) Deformed Shapes (Vertical vs. Lateral Deflection).** The deformed shapes showing the plots of the midspan vertical deflections vs. midspan lateral deflections for IPE 200 profile for a simply-supported beam of span length from 2.0 m to 6.0 m are shown in Figures 5.40 to 5.44.

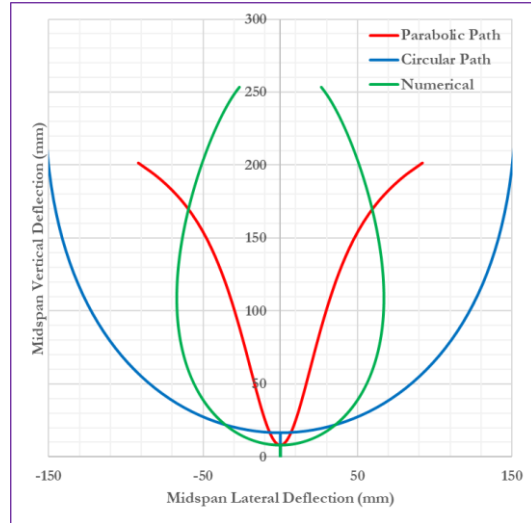


Figure 5.40. Vertical vs. Lateral Deflection for IPE 200 Profile with Span of 2.0 m.

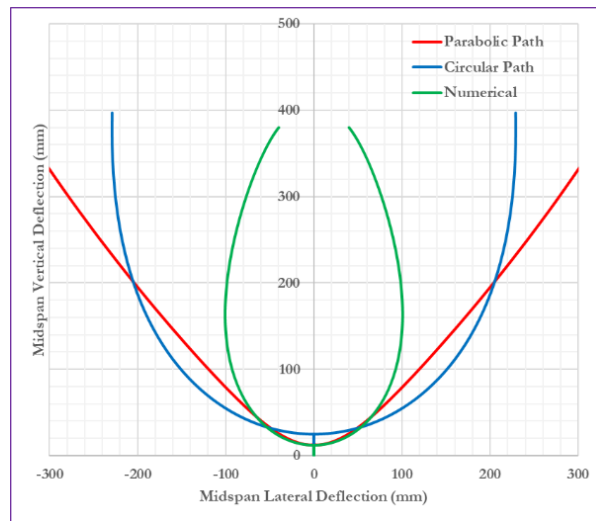


Figure 5.41. Vertical vs. Lateral Deflection for IPE 200 Profile with Span of 3.0 m.

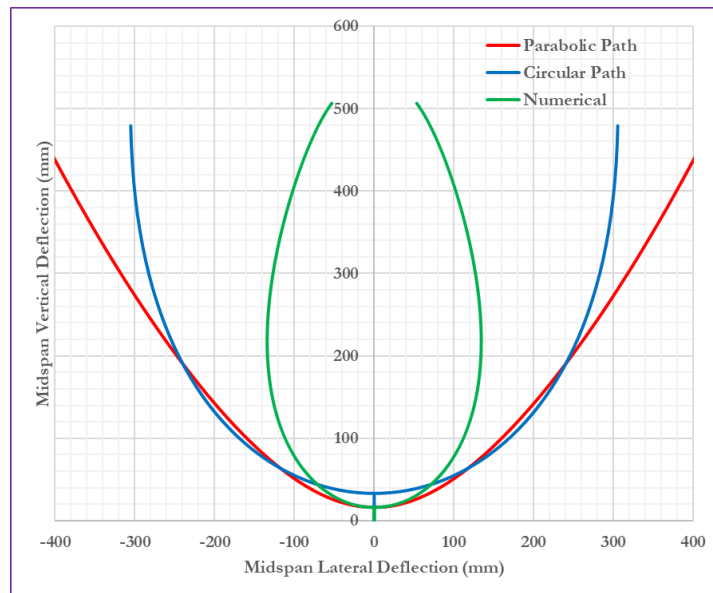


Figure 5.42. Vertical vs. Lateral Deflection for IPE 200 Profile with Span of 4.0 m.

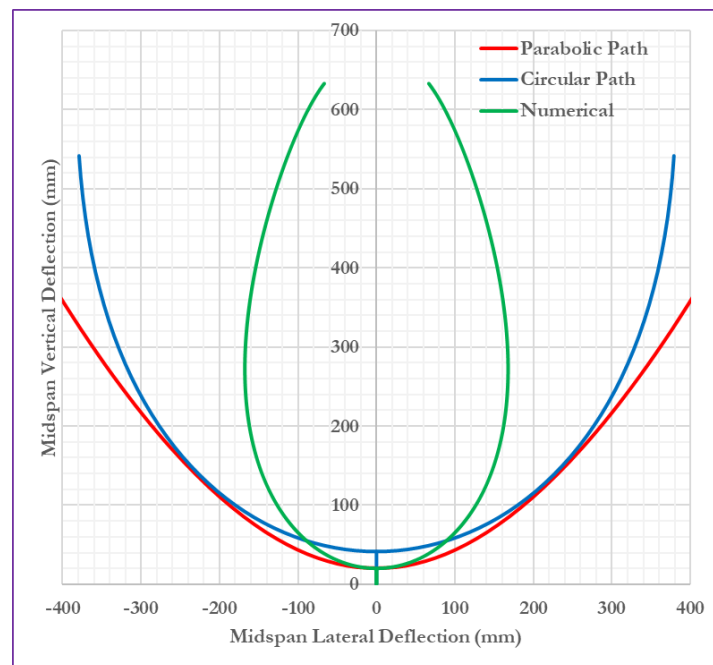
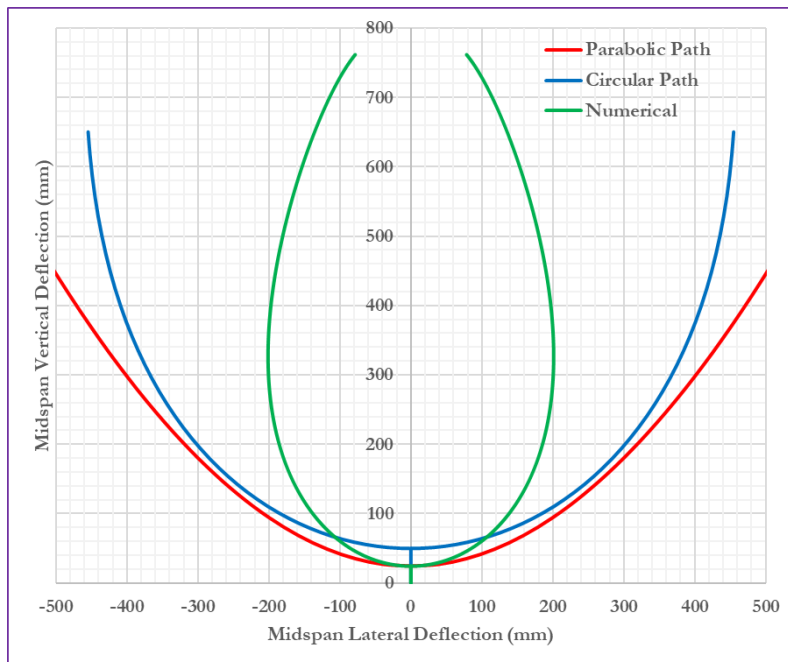


Figure 5.43. Vertical vs. Lateral Deflection for IPE 200 Profile with Span of 5.0 m.



**Figure 5.44. Vertical vs. Lateral Deflection for IPE 200 Profile with Span of 6.0 m.**

The deformed shapes, showing plot of vertical deflection vs lateral deflection, for the analytical method based on the circular deformation path completely disagree with the numerical solutions for all beam spans, even though they are qualitatively similar, as shown in Figures 5.40 to Figure 5.44.

As shown in Figure 5.40, the deformed shape in the post-buckling region of the analytical parabolic deformation path solution is above the numerical one for 2.0 m beam span and it slowly goes down as the span length increases ending up below the numerical deformed shape for longer beam spans, as shown in Figures 5.42 to 5.44 for 4.0 m to 6.0 m beam spans. The agreement between the deformed shapes from the analytical method based on the parabolic deformation path with the numerical one is different across different beam spans. The deformed shapes from the parabolic path have better initial matching in the post-buckling region with the numerical deformed shapes for a beam span of 3.0 m as shown in Figures 5.41. This matching in the deformed shapes doesn't exist for 2.0 m beam span as shown in Figures 5.40.

## 6.CONCLUSIONS AND RECOMMENDATIONS

### 6.1 SUMMARY AND CONCLUSIONS

This thesis aimed to examine the LTB and post-buckling behavior of simply-supported steel IPE beams subjected to midspan point loads with the specific objective of finding appropriate analytical model and expression to show the post-buckling behavior.

For this purpose, both analytical models based on assumed deformation paths (circular and parabolic) and nonlinear finite element analysis via OpenSeesPy are employed and a comprehensive comparison was made across various beam section sizes.

The analytical methods are grounded in idealized energy-based assumptions of deformation and provide valuable insight into the sensitivity of buckling behavior to path-dependent deformation modes. While these methods are mathematically rigorous and offer useful insight into idealized deformation behavior, they do not fully account for factors such as boundary conditions, shear deformations, or cross-section distortion.

Key conclusions include:

(a) **Critical Load Prediction.** All methods (Eurocode, OpenSeesPy and Analytical methods) predict increasing critical buckling loads with increasing IPE section size due to higher stiffness. The Eurocode yields the most conservative estimates with about 11% difference from the numerical results. The critical load prediction from the circular deformation path model is very high with nearly 105% difference from the numerical results. Therefore, the parabolic model with calibrated coefficient to give the same estimate of the critical load as the numerical solution is developed.

(b) **Post-Buckling Response Behavior.** The analytical circular path solution exhibits a consistent subcritical (softening) behavior, while the numerical solution and the analytical parabolic path solution show a supercritical response. This difference underscores the impact of the assumed deformation mode on capturing the real post-buckling path.

The analytical solutions have more pronounced divergence from the numerical results as the beam goes further to the post-buckling region. These might be the effect of geometric nonlinearity and second-order deformations which become more significant factors that

are not fully captured by the simplified analytical formulations. Plots of applied load versus midspan lateral deflection and torsional twist highlight these trends.

Overall based on the plot patterns the parabolic path shows better qualitative similarity with the numerical solution. For low to intermediate section sizes and longer spans the analytical lateral deflection estimates show better matching with the numerical solution in the early post-buckling region, while the vertical deflection estimates are analogous to the numerical solution in the early post-buckling region for medium section sizes and medium beam spans. The twist estimates show nearly perfect matching with the numerical solution for medium profiles and beam spans, although they show good agreement in the early post-buckling region for all section sizes and all beam spans.

**(c) Deformed Shape Agreement.** The deformed shape shown by lateral deflection–vertical deflection plots from the analytical circular path model completely disagree with the numerical solutions for all section sizes and beam spans, even though they are qualitatively similar, while the ones from the parabolic deformation path show improved similarity with the numerical deformed shapes for smaller to medium section sizes and medium to longer beam spans initially in the post-buckling region.

Overall, the study highlights the benefits and limitations of the simplified analytical models (circular and parabolic). While they offer valuable theoretical insight and quick estimations for initial buckling analysis of beams with higher stiffness, they must be used with caution, especially for small and flexible sections or detailed post-buckling analysis.

## 6.2 FUTURE WORK RECOMMENDATIONS

Based on the findings of this thesis, the following recommendations are proposed for future research and practical applications:

- Refine the parabolic deformation path assumption: Although it aligns better with numerical results, the parabolic deformation path assumption could be enhanced by calibrating it with more advanced deformation shape functions.
- Extend to other boundary conditions and loading types: This study focuses on simply-supported beams under point load. Future studies should explore different boundary conditions and loading scenarios (e.g., distributed load) to assess the generality of the analytical models
- Include warping effects into analytical models: The analytical formulations in this thesis neglect warping stiffness. Future work should include warping in the analytical models to improve accuracy. With further refinement for warping effects, it could serve as the basis for simplified design tools or charts for quick estimation of post-buckling behavior in engineering practice.

- Use experiments for validation: Although a comparison is done using numerical modelling in OpenSeesPy, experimental tests can be utilized in future studies to validate and refine simplified analytical approaches.
- Investigate material nonlinearities: This study assumes linear-elastic behavior. Incorporating material nonlinearities in both numerical and analytical analysis could provide deeper insights into the ultimate load-carrying capacity and ductility of beams.



## REFERENCES

- Andrade, A., Camotim, D., & Providência e Costa, P. (2007). On the evaluation of elastic critical moments in doubly and singly symmetric I-section cantilevers. *Journal of Constructional Steel Research*, 63(7), 894–908. <https://doi.org/10.1016/j.jcsr.2006.08.015>
- Bureau, A. (2005). NCCI: *Elastic Critical Moment for Lateral Torsional Buckling (SN003b-EN-EU)* (Nos SN003b-EN-EU; NCCI: Non-Contradictory Complementary Information, p. 14). Steel Construction Institute (SCI).
- EN 1993-1-1:2005—*Eurocode 3: Design of steel structures—Part 1-1: General rules and rules for buildings* (No. EN 1993-1-1:2005). (2005).
- Gonçalves, R. (2019). An assessment of the lateral-torsional buckling and post-buckling behaviour of steel I-section beams using a geometrically exact beam finite element. *Thin-Walled Structures*, 143, 106222. <https://doi.org/10.1016/j.tws.2019.106222>
- Koiter, W. T. (1945). *On the Stability of Elastic Equilibrium* [PhD Thesis]. Techische Hooge School.
- Nayak, N., Anilkumar, P. M., & Subramanian, L. (2024). Lateral-Torsional Buckling Modification Factors in Steel I-Shaped Members: Recommendations Using Energy-Based Formulations. *Engineering Journal*, 61(3). <https://doi.org/10.62913/engj.v61i3.1328>
- Nseir, J. (2023). Stability, failure and design of I-section steel beams subjected to tension. *Research and Applications in Structural Engineering, Mechanics and Computation*.
- Timoshenko, S. P., & Gere, J. M. (2012). *Theory of Elastic Stability*. Courier Corporation.

- Trahair, N. (1993). *Flexural-Torsional Buckling of Structures*. CRC Press.
- V. Z. Vlasov. (1961). *Thin Walled Elastic Beams*. IPST.
- Vila Real, P. M. M., Piloto, P. A. G., & Franssen, J.-M. (2003). A new proposal of a simple model for the lateral-torsional buckling of unrestrained steel I-beams in case of fire: Experimental and numerical validation. *Journal of Constructional Steel Research*, 59(2), 179–199.  
[https://doi.org/10.1016/S0143-974X\(02\)00023-8](https://doi.org/10.1016/S0143-974X(02)00023-8)

## APPENDIX A. EQUATION OF PARABOLIC PATH

Parabolic path of deflection shown by the red broken curve in Figure 3.5.

$$y = a \cdot z^2 + b \cdot z + c$$

Where: a, b and c are coefficients of the parabolic path of deflection.

Considering the bottom of the undeflected beam cross-section along its vertical axis of symmetry as the origin and the first point on the deflection-path with coordinate (0, 0).

Solving the deflection equation at the first point:

$$\begin{aligned} y(0, 0) = 0 &\Rightarrow a \cdot 0^2 + b \cdot 0 + c = 0 && \Rightarrow c = 0 \\ &\Rightarrow y = a \cdot z^2 + b \cdot z \end{aligned}$$

Since the arching point for the parabolic path occurs at the bottom of the undeformed beam section, it is possible to solve for the second coefficient b by taking derivative of y(z) and equating it to zero (i.e. Slope of y(z) is zero at the arching point).

$$\begin{aligned} \frac{dy}{dz}(0, 0) &= 0 \\ \frac{dy}{dz} &= \frac{d}{dz}(a \cdot z^2 + b \cdot z) = 2a \cdot z + b \\ \frac{dy}{dz}(0, 0) &= 0 \Rightarrow 2a \cdot 0 + b = 0 \Rightarrow b = 0 \\ &\Rightarrow y = a \cdot z^2 \end{aligned}$$

## APPENDIX B. NUMERICAL CODE IN OPENSEEESPY

```

#%matplotlib widget
import ipywidgets as widgets
from ipywidgets import interact
from sympy import *
from spb import plot_contour, plot3d, plot, graphics, line, plot3d_list
import numpy as np
import matplotlib.pyplot as plt
import openseespy.opensees as ops
import pandas as pd

#####
#####           DEFINE IPE SECTIONS           #####
#####

IPE_SECTIONS = {
    "IPE100": {"h": 100, "A": 1032, "Iy": 1.592e5, "Iz": 1.710e6, "It": 1.153e4, "Iw": 342.100e6},
    "IPE120": {"h": 120, "A": 1321, "Iy": 2.767e5, "Iz": 3.178e6, "It": 1.689e4, "Iw": 872.000e6},
    "IPE140": {"h": 140, "A": 1643, "Iy": 4.492e5, "Iz": 5.412e6, "It": 2.401e4, "Iw": 1951.00e6},
    "IPE160": {"h": 160, "A": 2009, "Iy": 6.831e5, "Iz": 8.693e6, "It": 3.530e4, "Iw": 3889.00e6},
    "IPE180": {"h": 180, "A": 2395, "Iy": 10.09e5, "Iz": 13.17e6, "It": 4.723e4, "Iw": 7322.00e6},
    "IPE200": {"h": 200, "A": 2848, "Iy": 14.24e5, "Iz": 19.43e6, "It": 6.846e4, "Iw": 12746.0e6},
    "IPE220": {"h": 220, "A": 3337, "Iy": 20.49e5, "Iz": 27.72e6, "It": 8.982e4, "Iw": 22310.00e6},
    "IPE240": {"h": 240, "A": 3912, "Iy": 28.36e5, "Iz": 38.92e6, "It": 12.74e4, "Iw": 36680.00e6},
    "IPE270": {"h": 270, "A": 4595, "Iy": 41.99e5, "Iz": 57.90e6, "It": 15.71e4, "Iw": 69469.00e6},
    "IPE300": {"h": 300, "A": 5381, "Iy": 60.38e5, "Iz": 83.56e6, "It": 19.75e4, "Iw": 124260.0e6},
    "IPE330": {"h": 330, "A": 6261, "Iy": 78.81e5, "Iz": 117.7e6, "It": 27.59e4, "Iw": 196090.0e6}
}

#####
#####           DEFINE BEAM LENGTHS           #####
#####

BEAM_LENGTHS = {
    "2.0 m": 2000.0,
    "3.0 m": 3000.0,
    "4.0 m": 4000.0,
    "5.0 m": 5000.0,
    "6.0 m": 6000.0
}

#####
#####           DROPODOWN OPTIONS           #####
#####

SECTION_DROPDOWN = widgets.Dropdown(options = IPE_SECTIONS.keys(), value = 'IPE330', description = 'SECTION:')
LENGTH_DROPDOWN = widgets.Dropdown(options = BEAM_LENGTHS.keys(), value = '4.0 m', description = 'LENGTH:')

def run_simulation(SECTION_CHOSEN, LENGTH_CHOSEN):

    #####
    #####           SELECTION OF SECTION AND LENGTH           #####
    #####
    SECTION_PROPERTY = IPE_SECTIONS[SECTION_CHOSEN]
    L = BEAM_LENGTHS[LENGTH_CHOSEN]

    #####
    #####           GEOMETRIC PROPERTIES           #####
    #####
    h = SECTION_PROPERTY["h"]
    A = SECTION_PROPERTY["A"]
    Iy = SECTION_PROPERTY["Iy"]
    Iz = SECTION_PROPERTY["Iz"]
    It = SECTION_PROPERTY["It"]
    Iw = SECTION_PROPERTY["Iw"]

    #####
    #####           MATERIAL PROPERTIES AND CONSTANTS           #####
    #####
    E = 200000 # MPa
    G = 80000 # MPa

```

```
#####
# OPENSEES OR NUMERICAL SIMULATION #####
ops.wipe()
ops.model('basic', '-ndm', 3, '-ndf', 6)

ops.node(1, 0, 0, 0)
ops.node(2, L/2, 0, 0.00001)
ops.node(3, L, 0, 0)

ops.fix(1, 1, 1, 1, 0, 0)
ops.fix(3, 0, 1, 1, 1, 0, 0)

ops.geomTransf('Corotational', 1, 0, 1, 0)
ops.uniaxialMaterial('Elastic', 1, E)
ops.section('Elastic', 1, E, A, Iy, Iz, G, It)

ops.element('elasticBeamColumn', 1, 1, 2, 1, 1)
ops.element('elasticBeamColumn', 2, 2, 3, 1, 1)

ops.timeSeries('Linear', 1)
ops.pattern('Plain', 1, 1)
ops.load(2, 0.0, -1.0, 0.0, 0.0, 0.0, 0.0)

ops.system('BandGeneral')
ops.numberer('RCM')
ops.constraints('Plain')
ops.test('NormDispIncr', 1.0e-6, 300)
ops.algorithm('Newton')
ops.integrator('ArcLength', 1.0, 1.0)
ops.analysis('Static')

applied_forces = []
vertical_deflections = []
lateral_deflections = []
torsional_twists = []

for step in range(400000):
    ok = ops.analyze(1)
    if ok != 0:
        break
    lf = ops.getLoadFactor(1)
    uy = ops.nodeDisp(2, 2)
    uz = ops.nodeDisp(2, 3)
    rx = ops.nodeDisp(2, 4)

    applied_forces.append(lf)
    vertical_deflections.append(uy)
    lateral_deflections.append(uz)
    torsional_twists.append(rx)

widgets.interact(run_simulation, SECTION_CHOSEN = SECTION_DROPDOWN, LENGTH_CHOSEN = LENGTH_DROPDOWN)
```